Chapter 7

Decay and Amplification of Magnetic Fields

It's not whether a thing is hard to understand.
It's whether, once understood, it makes any sense.

Hans Zinsser
Rats, Lice and History (1934)

We now begin our long modelling journey towards astrophysical dynamos. It is a road long and hard and, n'en déplaise à Nick Cave, we would like to avoid too many falling by the side. Consequently this chapter will for the most part concentrate on a series of (relatively) simple model problems illustrating the myriad of manners in which a flow and a magnetic field can interact. We will first consider the purely resistive decay of magnetic fields (§7.1) [1], then examine various circumstances under which stretching by a flow can amplify a magnetic field (§7.2), and then examine some important subtleties of this process in the context of some (relatively) simple 2D flows (§7.3). The chapter close with some so-called anti-dynamo theorems (§7.4), which will shed light on results from previous sections and indicate the way towards true magnetohydrodynamical dynamo action, which, I may as well admit it at the onset, we will first encounter only in the next chapter. Some of the material contained in this chapter may feel pretty far remote from the realm of astrophysics at times, but please do stick to it because the physical insight (hopefully) developed in the following sections will prove essential to pretty much everything that will come next.

7.1 Resistive decays of magnetic fields

Before we try to come up with flows leading to field amplification and dynamo action, we better understand the enemy, namely magnetic field decay by Ohmic dissipation. Consequently, we first consider the evolution of magnetic fields in a conducting fluid, in the absence of any fluid motion (or, more generally, in the $R_m \ll 1$ limit). The induction equation then reduces to

$$\frac{\partial \mathbf{B}}{\partial t} = -\nabla \times (\eta \nabla \times \mathbf{B}) = \eta \nabla^2 \mathbf{B} - (\nabla \eta) \times (\nabla \times \mathbf{B}) \ . \tag{7.1}$$

Were it not that we are dealing here with a vector —as opposed to scalar— quantity, for constant η this would look just like a simple heat diffusion equation, with η playing the role of thermal diffusivity. Way, way back in chapter 1 we already obtained an order-of-magnitude estimate for the timescale τ_η over which a magnetic field $\mathbf{B}$ with typical length scale ℓ can be

[1] With the exception of §7.1.4, all of this section was written by Thomas J. Bogdan.

expected to resistively decay:

$$\tau_\eta \sim \frac{\ell^2}{\eta} \ . \tag{7.2}$$

which in the case of the solar interior ended up at $\tau \sim 10^{10}\,\mathrm{yr}$, i.e., about the main-sequence lifetime of the Sun. You should also recall that this is due primarily to the large spatial scale of the system, as opposed to an exceedingly low diffusivity. The *existence* of a solar magnetic field is then not really surprising; any large-scale fossil field present in the Sun's interior upon its arrival on the ZAMS would still be there today at almost its initial strength. The challenge in modeling the solar magnetic field is to reproduce the peculiarities of its spatial and temporal variations, in particular the cyclic variation of its large-scale component on a $\sim 22\,\mathrm{yr}$ timescale. But we are getting ahead of ourselves here. Back to simple resistive decay.

7.1.1 Reformulation as an eigenvalue problem

Let us now seek specific solutions for a few situations of solar interest, and (hopefully) verify our estimate of 10^{11} yr for the decay time of a fossil solar magnetic field. We are free to work directly with the magnetic induction equation for $\mathbf{B}$ (eq. (6.24)), or the "uncurled" equation for the vector potential $\mathbf{A}$ (eq. (1.105)). Choosing here the latter route, the magnetic and electric fields are obtained from the relations

$$\mathbf{B} = \nabla \times \mathbf{A} \ , \qquad \mathbf{E} = -\frac{1}{c}\frac{\partial \mathbf{A}}{\partial t} \ . \tag{7.3}$$

The first point to notice is that the coefficients that appear in eq. (1.3) are independent of time, and so it is profitable to seek a separable solution of the form,

$$\mathbf{A} = e^{\lambda t}\mathbf{A}_\lambda(\mathbf{r}) \ , \quad \Phi = e^{\lambda t}\Phi_\lambda(\mathbf{r}) \ . \tag{7.4}$$

The decay rate, λ, is then determined by the eigenvalue problem,

$$\lambda \mathbf{A}_\lambda + \eta \nabla \times (\nabla \times \mathbf{A}_\lambda) = c\nabla \Phi_\lambda \ , \tag{7.5}$$

along with some appropriate boundary conditions that we shall presently get to. We are still carrying the electrostatic potential Φ along just to keep matters as general as possible, but we shall make every effort to rid ourselves of this encumberance as soon as the opportunity presents itself.

The LHS of eq. (7.5) is the vector-Helmholtz equation which arises routinely in the description of electromagnetic wave propagation problems.[2] Therefore we should take advantage of the hard work others have done in order to make our present task easy. The elegant way to proceed is to define three vector operators which act upon scalar functions of $\mathbf{r}$ according to the prescriptions,

$$\mathbf{T} = -\hat{\mathbf{e}}_r \times \nabla \ , \qquad \mathbf{P} = -\nabla \times (\mathbf{r} \times \nabla) \ , \qquad \mathbf{L} = \nabla \ , \tag{7.6}$$

and generate *toroidal*, *poloidal*, and *longitudinal* vector fields, respectively.[3] We now construct $\mathbf{A}$ from these operators and three scalar functions according to,

$$\mathbf{A}_\lambda = r\mathbf{T}[\alpha_\lambda] + \mathbf{P}[\beta_\lambda] + \mathbf{L}[\gamma_\lambda] \ . \tag{7.7}$$

The benefit of all this is that the three vector operators have very nice transformation properties under the action of the curl operator,

$$\nabla \times r\mathbf{T} = \mathbf{P} \ , \qquad \nabla \times \mathbf{P} = -r\mathbf{T}\nabla^2 \ , \qquad \nabla \times \mathbf{L} = 0 \ , \tag{7.8}$$

[2] Verify that Maxwell's equations in vacuum reduce to eq. (7.5) with $\eta = 1$ and $\lambda = -\omega^2/c^2$.

[3] The prescription presented here is for spherical coordinates. For other coordinate systems one replaces $\mathbf{r}$ and $\hat{\mathbf{e}}_r$ by the relevant vectors.

where $\nabla \cdot \mathbf{L} = \nabla^2$ is the Laplacian, and $\nabla \cdot \mathbf{T} = \nabla \cdot \mathbf{P} = 0$.

It is now straightforward bookkeeping to substitute this representation for $\mathbf{A}_\lambda$ into eq. (7.5), collect similar looking terms, and arrive at the following set of uncoupled equations,

$$\lambda\alpha_\lambda = \nabla^2\alpha_\lambda \ , \tag{7.9}$$

$$\lambda\beta_\lambda = \nabla^2\beta_\lambda \ , \tag{7.10}$$

$$\lambda\gamma_\lambda = c\Phi_\lambda \ , \tag{7.11}$$

provided η is at worst only function of the radius r. The first two of these expressions are identical to the *scalar* Helmholtz equation encountered in the study of stellar oscillations. We recall that the spherical harmonics are the canonical angular functions that span the surface of a sphere. And so we may write either α_λ or β_λ as the product,

$$f_\lambda(r) Y_{lm}(\Omega) \ , \tag{7.12}$$

for any non-negative integer l. The remaining unknown function and the much-anticipated eigenvalue λ are determined by the resulting ODE,

$$\Big[\frac{1}{r^2}\frac{\mathrm{d}}{\mathrm{d}r}r^2\frac{\mathrm{d}}{\mathrm{d}r} - \frac{l(l+1)}{r^2} + \frac{\lambda}{\eta(r)}\Big] f_\lambda(r) = 0 \ . \tag{7.13}$$

By virtue of the second term on the LHS of this equation, $r = 0$ is a singular point of this ODE and accordingly the non-analytic of the two linearly-independent solutions about this point must be discarded to maintain a sensible physical solution. The freedom to choose λ is necessary to force the remaining analytic solution to satisfy a prescribed boundary condition at the surface of the star ($r = R$). The nature of this boundary condition depends sensitively on the vector character of the decaying magnetic field.

7.1.2 Poloidal field decay

A poloidal magnetic field is generated by the $\alpha_\lambda(\mathbf{r})$ function. Hence, if we set $\beta_\lambda = 0$ we obtain,

$$\mathbf{B}_\lambda = \mathbf{P}[\alpha_\lambda] \ , \mathbf{E}_\lambda = -\frac{\lambda}{c}\Big\{r\mathbf{T}[\alpha_\lambda] + \mathbf{L}[\gamma_\lambda]\Big\} \ , \tag{7.14}$$

valid for $r \neq R$. In the vaccuum surrounding the star $\eta = \infty$ since no material currents are allowed to be present, and Maxwell's displacement current has also been neglected. In this region we have the familiar potential field with $\alpha_\lambda \propto (R/r)^{l+1} Y_{lm}(\Omega)$. Inside the star, $\eta \neq \infty$, and the radial dependence of α_λ follows from the eigenvalue ODE, eq. (7.13).

Examination of the components of the $\mathbf{P}$ operator indicates that α_λ must be continuous across the stellar surface, $r = R$, else $\mathbf{B}$ will not be defined there. This can be accommodated through the freedom to multiply the exterior potential field solution by an arbitrary constant. So λ is still undetermined.

The current density (and hence the electric field) are given by the curl of the magnetic field. For $\mathbf{E}$ to be well-defined on the surface $r = R$ as the appropriate limit of the interior and exterior solutions, $\mathbf{B}$ must be continuous across the stellar surface. Since both the interior and exterior solutions carry the common factor of $Y_{lm}(\Omega)$, this is achieved merely by having $\partial\alpha_\lambda/\partial r$ continuous across $r = R$. As λ is the only thing left at our disposal to make this happen, the eigenvalue, and the decay-rate, are thus so-determined.

To see how this plays out, assume $\eta = \eta_0$ is constant throughout the interior of the star. The appropriate radial dependence within the star is describes by a spherical Bessel function, i.e.,

$$\alpha_\lambda = Y_{lm}(\Omega) j_l(kr) \qquad r < R \tag{7.15}$$

$$\alpha_\lambda = Y_{lm}(\Omega) j_l(kR)\Big(\frac{R}{r}\Big)^{l+1} \qquad r > R \tag{7.16}$$

where $k^2 \equiv \lambda/\eta_0$. The continuity of the radial derivative is assured if

$$kRj_l'(kR) + (l+1)j_l(kR) = kRj_{l-1}(kR) = 0 \ , \tag{7.17}$$

and so one need only hunt for the zeros of a spherical Bessel function in order to determine the decay rate of a poloidal magnetic field! An $l = 1$ dipole calls for the positive zeros of $j_0(x) = \sin x/x$. These are simply integer multiples of π, thus

$$\lambda_n = \frac{\eta_0 \pi^2 n^2}{R^2} \ , \qquad \text{for } l = 1 \ , n = 1, 2, 3, ... \tag{7.18}$$

Notice the many possible *overtones* associated with $n \geq 2$. These decay more rapidly than the fundamental ($n = 1$), since the radial eigenfunctions possess $n - 1$ field reversals. For such overtones, the effective length scale to be used in the decay-time estimate is roughly the radial distance between the field reversals, or $\approx R/n$.

Figure 7.1 (top row) shows the first three fundamental ($n = 1$) modes of angular degrees $l = 1, 2, 3$, corresponding to dipolar, quadrupolar, an hexapolar magnetic fields, as well as a few higher overtones for $l = 1, 2$ (bottom row). It is worth noting that the azimuthal quantum number, m, has no impact on computed decay rate. And last, but not least, the fossil field lifetime estimate provided by eq. (7.2) is just a little on the large side, by a factor of $\pi^2 \approx 10$, for a sun with constant diffusivity.

And what about γ_λ? Since everyone is continuous and well-defined there is no need for it, i.e., $\gamma_\lambda = \Phi_\lambda = 0$![4]

7.1.3 Toroidal field decay

How about the decay rate of a purely toroidal magnetic field? The general approach remains the same, but now we can zero-out α_λ, giving

$$\mathbf{B}_\lambda = -r\mathbf{T}[\nabla^2 \beta_\lambda] \ , \mathbf{E}_\lambda = -\frac{\lambda}{c}\Big\{\mathbf{P}[\beta_\lambda] + \mathbf{L}[\gamma_\lambda]\Big\} \ , \tag{7.19}$$

again, valid for $r \neq R$. Everywhere *except* on the stellar surface, we can make good use of the fact that,

$$\nabla^2 \beta_\lambda = \frac{\lambda}{\eta(r)} \beta_\lambda \ . \tag{7.20}$$

In the surrounding vacuum, $\eta = \infty$, and so as before, $\beta_\lambda \propto (R/r)^{l+1} Y_{lm}(\Omega)$, for $r > R$. *Howeve*r, in this case, the consequence is that $\mathbf{B} = 0$ for $r > R$. Continuity of $\mathbf{B}$ at the stellar surface now demands that *both* β_λ *and* its radial derivative be continuous on $r = R$. The additional requirement that $\mathbf{B}$ be first-order differentiable (to avoid infiinite current densities at $r = R$) is what ends up determining the eigenvalue λ.

The decay rate λ^{-1} is again related to the zero of a spherical Bessel function—only of index l rather than $l - 1$ as was found for the decay of the poloidal field. Hence, a dipole ($l = 1$) toroidal magnetic field decays at precisely the same rate as a quadrupole ($l = 2$) poloidal magnetic field (at least for constant diffusivity)! As before, the azimuthal quantum number m remains a non-issue. Looking up the expression for $j_1(x)$ in your favorite tome on special functions, the decay rate of a dipole toroidal field follows from the transcendental equation,

$$\tan kR = kR \ . \tag{7.21}$$

The smallest non-zero solution of this equation gives,

$$\lambda_1 = \frac{\eta_0 (4.493409...)^2}{R^2} \ , \qquad l = 1 \text{ toroidal and } l = 2 \text{ poloidal.} \tag{7.22}$$

[4] In fact, eq. (7.13) is readily obtained by adopting the mixed poloidal/toroidal axisymmetric ($m = 0$) formulation of §1.12.3, and setting $B = 0$ and $A(r, \theta, t) = f_\lambda(r) Y_{l0}(\cos\theta) e^{\lambda t}$. But the formulation developed in this section remains of far greater applicability since it is not restricted to axisymmetric magnetic fields.

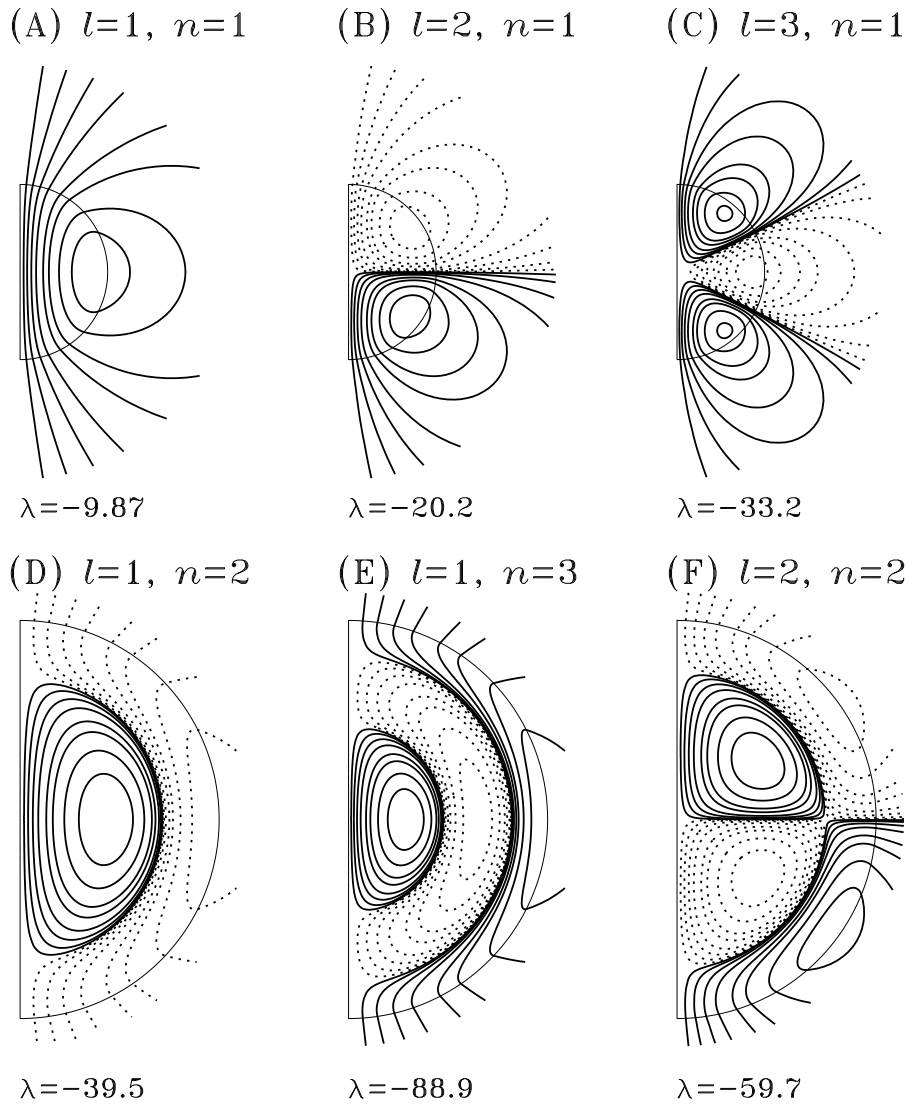

Figure 7.1: Six diffusive eigenmodes for a purely poloidal field pervading a sphere of constant magnetic diffusivity embedded in vacuum. The top row shows the three fundamental ($n = 1$) diffusive eigenmodes with smallest eigenvalues, i.e., largest decay times. They correspond to the well-known dipolar, quadrupolar, and hexapolar modes ($l = 1, 2$ and 3). The bottom row shows a few eigenmodes of higher radial overtones. Poloidal fieldlines are shown in a meridional plane, and the eigenvalues are given in units of the inverse diffusion time ($\tau^{-1} \sim \eta/R^2$).

It is worth a final remark to point out that the correct decay rate for a toroidal field would have been obtained merely from solving eq. (7.1) in the mixed representation by setting $A = 0$ and forcing B to vanish at $r \gtrsim R$. But then, think of all the subtleties and fun that would have been missed!

7.1.4 Results for a magnetic diffusivity varying with depth

We end this section by a brief examination of the diffusive decay of large-scale poloidal magnetic fields in the solar interior. The primary complication centers on the magnetic diffusivity, which is no longer constant throughout the domain, and turns out to be rather difficult to compute from first principles[5]. To begin with, the depth variations of the temperature and density in a solar model causes the magnetic diffusivity to increase from about $10^{-2}\,\mathrm{m^2 s^{-1}}$ in the central core to $\sim 1\,\mathrm{m^2 s^{-1}}$ at the core-envelope interface. This already substantial variation is however dwarfed by the much larger increase in the net magnetic diffusivity expected in the turbulent environment of the convective envelope. We will look into this in some detail in chapter 9, but for the time being let us simply take for granted that η is much larger in the envelope than in the core.

In order to examine the consequences of a strongly depth-dependent magnetic diffusivity on the diffusive eigenmodes, we consider a simplified situation whereby η assumes a constant value η_c in the core, a constant value η_e ($\gg \eta_c$) in the envelope, the transition occurring smoothly across a thin spherical layer coinciding with the core-envelope interface. Mathematically, such a variation can be expressed as

$$\eta(r) = \eta_c + \frac{\eta_e - \eta_c}{2}\left[1 + \mathrm{erf}\left(\frac{r - r_c}{w}\right)\right], \tag{7.23}$$

where $\mathrm{erf}(x)$ is the error function, r_c is the radius of the core-envelope interface, and w is the half-width of the transition layer.

We are still facing the 1D eigenvalue problem presented by eq. (7.13)! Expressing time in units of the diffusion time R^2/η_e based on the envelope diffusivity, we seek numerical solutions, subjected to the boundary conditions $f_\lambda(0) = 0$ and smooth matching to a potential field solution in $r/R > 1$, with the diffusivity ratio $\Delta\eta = \eta_c/\eta_e$ as a parameter of the model. Since we can make a reasonable guess at the eigenvalue on the basis of the diffusion time and adopted values of l and η_c ($\sim \pi^2 l n \Delta\eta$, for l and n not too large), inverse iteration (see Appendix F) is the technique of choice.

Figure 7.2 shows the radial eigenfunctions for the slowest decaying poloidal eigenmodes ($l = 1$, $n = 1$), with $r_c/R = 0.7$, $w/R = 0.05$ in eq. (7.23) and diffusivity contrasts $\Delta\eta = 1$ (constant diffusivity), 10^{-1} and 10^{-3}. The corresponding eigenvalues, in units of R^2/η_e, are $\lambda = -9.87$, -2.14 and -0.028. Clearly, the (global) decay time is regulated by the region of *smallest* diffusivity, since λ scales approximately as $(\Delta\eta)^{-1}$. Notice also how the eigenmodes are increasingly concentrated in the core region ($r/R \lesssim 0.7$) as $\Delta\eta$ decreases, i.e., they are "expelled" from the convective envelope. This is sometimes called the **diamagnetic effect** in the astrophysical literature. It has interesting consequences for models of the solar dynamo, and will be encountered again in later chapters.

The marked decrease of the diffusive decay time with increasing angular and radial degrees of the eigenmodes is a noteworthy result. It means that left to decay long enough, any arbitrarily complex magnetic field in the Sun or stars will eventually end up looking dipolar[6]. Conversely, a fluid flow acting as a dynamo in a sphere and trying to "beat" Ohmic dissipation can be expected to prefentially produce a magnetic field approximating diffusive eigenmodes of low angular and radial degrees (or some combination thereof), since these are the least sensitive to Ohmic dissipation.

[5] See the bibliography at the end of this chapter for some references.

[6] Is this always true? Can you think of circumstances where this would not be the case?

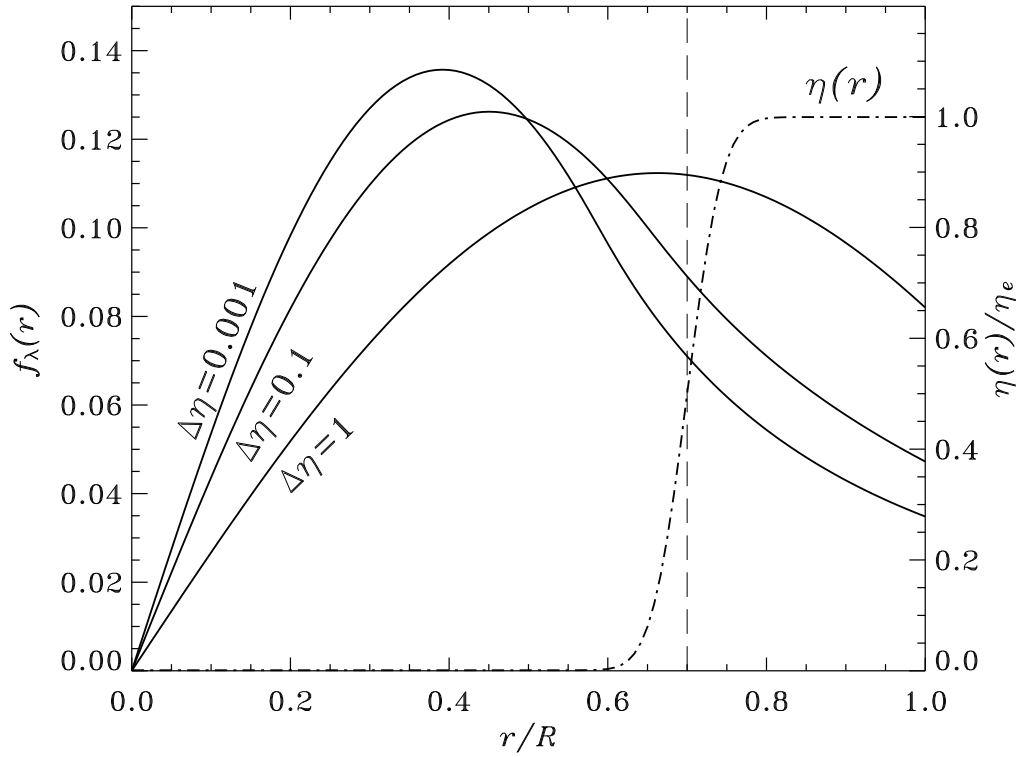

Figure 7.2: Radial eigenfunctions for the slowest decaying ($\ell = 1$) poloidal eigenmodes ($l = 1$, $n = 1$) in a sphere embedded in a vacuum. The diffusivity computed using eq. (7.23) with $r_c/R = 0.7$, $w/R = 0.05$, and for three values of the core-to-envelope diffusivity ratio ($\Delta\eta$). The eigenvalues, in units of η_e/R^2, are $\lambda = -9.87$, -2.14 and -0.028 for $\Delta\eta = 1$, 0.1, and 10^{-3}, respectively. The diffusivity profile for $\Delta\eta = 10^{-3}$ is also plotted (dash-dotted line). The dashed line indicates the location of the core-envelope interface.

There exists classes of early-type main-sequence stars, i.e. stars hotter and more luminous than the Sun and without deep convective envelope, that are believed to contain strong, large-scale fossil magnetic fields left over from their contraction toward the main-sequence. The chemically peculiar Ap stars are the best studied class of such objects. Reconstruction of their surface magnetic field distribution suggests almost invariably that the fields are largely dominated by the dipole component, as one would have expected from the preceding discussion if the observed magnetic fields have been diffusively decaying for tens or hundreds of millions of years[7].

7.2 Magnetic field amplification by stretching and shearing

Having now investigated in some the details the resistive decay of magnetic field, we turn to the other physical mechanism embodied in eq. (6.24): growth of the magnetic field in response to the inductive action of a flow $\mathbf{u}$. We first take a quick look at field amplification in a few idealized model, and in the next section move on to a specific example using a "real" flow.

[7]Care is warranted in making such conclusions on the basis of stellar observations, as the current techniques used to infer the presence and structure of the surface fields, based on Zeeman splitting and/or polarization of starlight, are significant biased towards the lower multipoles because the stellar surface remains spatially unresolved.

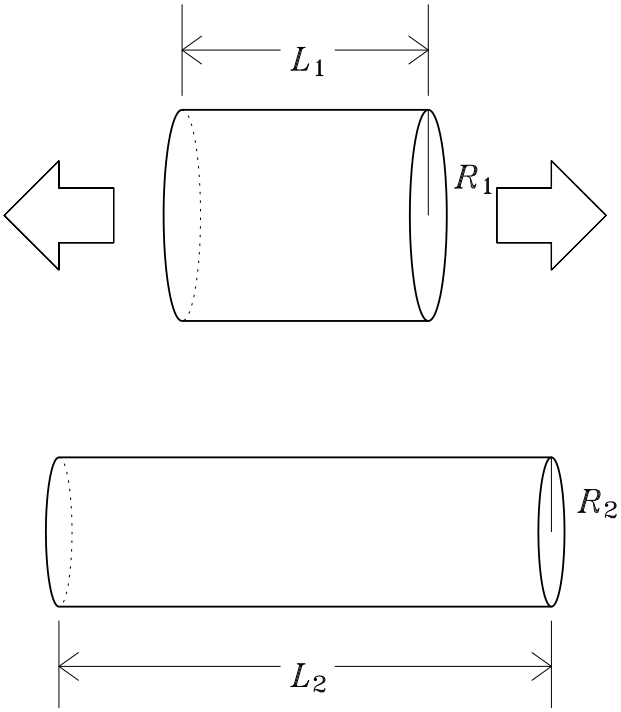

Figure 7.3: Stretching of a magnetized cylindrical fluid element by a diverging flow. The magnetic field is horizontal within the tube, has a strength B_1 originally, and B_2 after stretching. In the flux-freezing limit mass conservation within the tube requires its radius to decrease, which in turn leads to field amplification (see text).

7.2.1 Hydrodynamical stretching and field amplification

Let's revert for a moment to the ideal MHD case ($\eta = 0$). The induction equation can then expressed as

$$\frac{\partial \mathbf{B}}{\partial t} + (\mathbf{u} \cdot \nabla)\mathbf{B} = \mathbf{B} \cdot \nabla \mathbf{u} \ , \tag{7.24}$$

where it was further assumed that the flow is incompressible ($\nabla \cdot \mathbf{u} = 0$). The LHS of eq. (7.24) is the Lagrangian derivative of $\mathbf{B}$, expressing the time rate of change of $\mathbf{B}$ in a fluid element moving with the flow. The RHS expresses the fact that this rate of change is proportional to the local **shear** in the flow field. Shearing has the effect of **stretching** magnetic fieldlines, which is what leads to magnetic field amplification.

As a simple example, consider on Figure 7.3 a cylindrical fluid element of length L_1, threaded by a magnetic field parallel to the axis of the cylinder, imbedded in a perfectly conducting incompressible fluid and subjected to a stretching motion ($\partial u_x/\partial x > 0$) along its central axis such that its length increases to L_2. Mass conservation demands that $R_2/R_1 = \sqrt{L_1/L_2}$. Conservation of the magnetic flux ($= \pi R^2 B$) in turn leads to

$$\frac{B_2}{B_1} = \frac{L_2}{L_1} \ , \tag{7.25}$$

i.e., the field strength is amplified in direct proportion to the level of stretching. This almost trivial result is in fact at the very heart of *any* magnetic field amplification in the magnetohydrodynamical context, and illustrates two crucial aspects of the mechanism: first, this works only

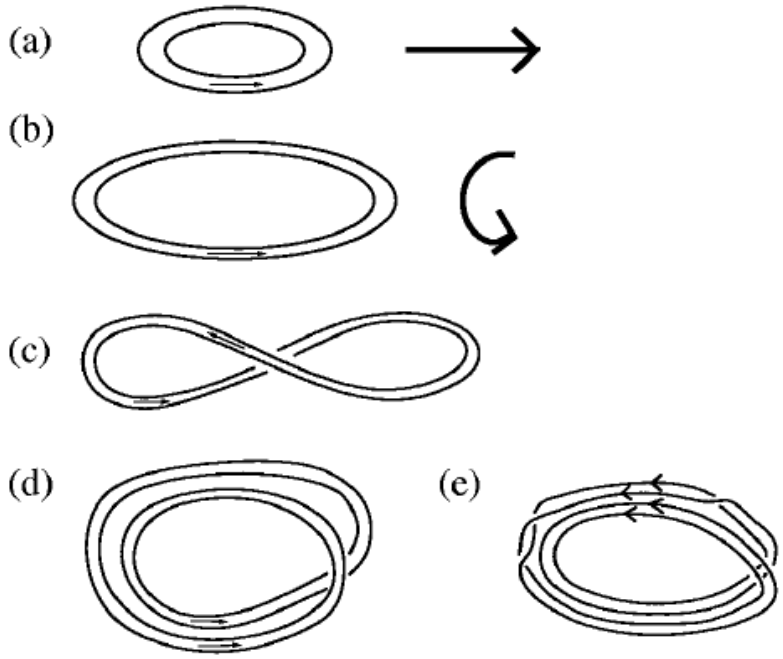

Figure 7.4: Cartoon of the Strech-Twist-Fold flux rope dynamo of Vainshtein & Zeldovich. A circular flux rope (a) is (b) stretched, (c) twisted, and (d) folded. Diagram (e) shows the resulting structure after another such step. Diagram digitized straight out of A.D. Gilbert's excellent dynamo review listed in the bibliography.

if the fieldlines are frozen into the fluid, i.e., in the high-R_m regime. Second, mass conservation plays an essential role here; the stretching motion along the tube axis *must* be accompanied by a compressing fluid motion perpendicular to the axis if mass conservation is to be satisfied. It is this latter compressive motion, occurring perpendicular to the magnetic fieldlines forming the flux tube, that is ultimately responsible for field amplification; the horizontal motion occurs parallel to the magnetic fieldline, and so cannot in itself have any inductive effect as per eq. (6.24)[8]. The challenge, of course, is to realize this idealized scenario in practice, i.e., to find a flow which achieves the effect illustrated on Figure 7.3.

7.2.2 The Vainshtein & Zeldovich flux rope dynamo

As trivial as the above example may appear, it can form the basis of a dynamo. S. Vainshtein and Ya. B. Zeldovich have proposed one of the first and justly celebrated "cartoon" model for this idea, as illustrated on Figure 7.4. The steps are the following:

1. A circular rope of magnetic field is stretched to twice its length ($a \to b$). As we just learned, this doubles the magnetic field strength;

2. The rope is twisted by half a turn ($b \to c$);

3. One half of the rope is folded over the other half in such a way as to align the magnetic field of each half ($c \to d$).

Clearly, this so-called **stretch-twist-fold** sequence (hereafter STF) doubles the field strength while conserving the total cross-section of the original rope, so that the magnetic flux is also

[8]Hold it now, how do you reconcile this statement with eq. (7.24), which indicates rather unambiguously that one can have $\partial \mathbf{B}/\partial t > 0$ with $\mathbf{B} = B_x \hat{\mathbf{e}}_x$ and $\mathbf{u} = u_x(x)\hat{\mathbf{e}}_x$?

doubled. If the sequence is repeated n times, the magnetic field strength (and flux) is then amplified by a factor

$$\frac{B^n}{B_0} \propto 2^n = \exp(n \ln 2) \ , \tag{7.26}$$

with n playing the role of a (discrete) time-like variable, eq. (7.26) indicates an exponential growth of the magnetic field, with a growth rate $\sigma = \ln 2$. Rejoyce! This is our first dynamo!

A concept central to the STF dynamo —and other dynamos to be encountered later— is that of **constructive folding**. Note how essential the twisting step is to the STF dynamo: without it (or with an even number of twists), the magnetic field in each half of the folded rope would end up pointing in opposite direction, and would then add up to zero net flux, a case of **destructive folding**. We'll have a more to say on the STF dynamo in the following chapter; for now we switch gears to consider a mechanism of field amplification of more obvious astrophysical relevance.

7.2.3 Toroidal field production by differential rotation

A situation of great (astro)physical interest is the induction of a toroidal magnetic field via the shearing of a poloidal magnetic field threading a differentially rotating sphere of electrically conducting fluid. Assuming axisymmetry (i.e., the poloidal field and differential rotation share the same symmetry axis) and neglecting once again magnetic dissipation, the induction equation take on the reduced form[9]

$$\frac{\partial A}{\partial t} = 0 \ , \tag{7.27}$$

$$\frac{\partial B}{\partial t} = \varpi[\nabla \times (A\hat{\mathbf{e}}_\phi)] \cdot \nabla\Omega \ . \tag{7.28}$$

where we took advantage of the poloidal/toroidal separation discussed in §1.12.3. For a steady rotation profile, equation (7.28) integrates immediately to

$$B(r,\theta,t) = B(r,\theta,0) + \Big(\varpi[\nabla \times (A\hat{\mathbf{e}}_\phi)] \cdot \nabla\Omega\Big)t \ . \tag{7.29}$$

Anywhere in the domain, the toroidal component of the magnetic field grows linearly in time, at a rate proportional to the net local shear and local poloidal field strength[10]. A toroidal magnetic component is being generated by *stretching* the initially purely poloidal fieldlines in the ϕ-direction; the magnitude of the poloidal magnetic component remains unaffected, as per eq. (7.27)!

Evidently computing B via eq. (7.29) requires a knowledge of the solar internal (differential) rotation profile $\Omega(r,\theta)$. Consider the following parametrization:

$$\Omega(r,\theta) = \Omega_C + \frac{\Omega_S(\theta) - \Omega_C}{2}\left[1 + \mathrm{erf}\left(\frac{r - r_C}{w}\right)\right] \ , \tag{7.30}$$

where

$$\Omega_S(\theta) = \Omega_{Eq}(1 - a_2\cos^2\theta - a_4\cos^4\theta) \tag{7.31}$$

is the surface latitudinal differential rotation. We will make repeated use of this parametrization in this and following and chapters, so let's look into it in some detail. Figure 7.5 shows a 2D helioseismic inversion of the solar internal rotation, together with the profile $\Omega(r,\theta)$ generated using the above expressions with parameter values $\Omega_C/2\pi = 432.8\,\mathrm{nHz}$, $\Omega_{Eq}/2\pi = 460.7\,\mathrm{nHz}$, $a_2 = 0.1264$, $a_4 = 0.1591$, $r_c = 0.713R$, and $w = 0.05R$. The degree of similarity with the "real" Sun is quite reasonable. Note in particular that both profiles are characterized by:

[9] Work it out!

[10] How long would it take for the solar differential rotation to shear a 1 G poloidal field into a 10^5 G toroidal field?

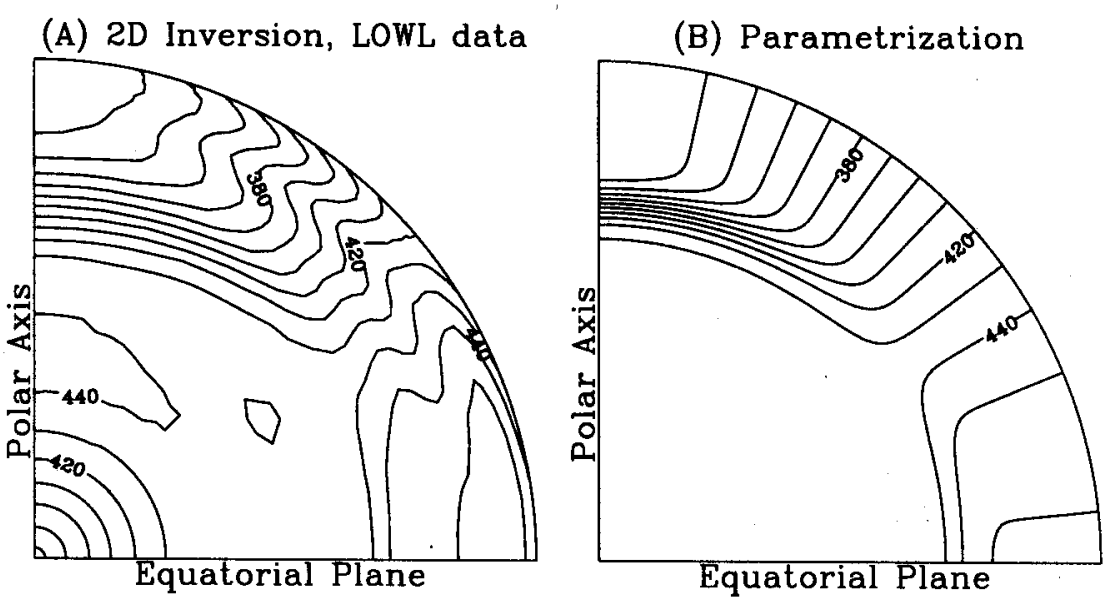

Figure 7.5: Regularized least-square inversion for the internal solar angular velocity, obtained with the LOWL 2-year frequency splitting dataset (left), and parametric representation obtained from eqs. (7.30) —(7.31) (right). The angular velocity is shown in a meridional quadrant, in the form of of angular *frequency*, in the range $340 \leq \Omega/2\pi \leq 460\,\mathrm{nHz}$ with 10 nHz spacing.

1. A convective envelope ($r \gtrsim r_c$) where the shear is purely latitudinal, with the equatorial region rotating faster than the poles;

2. A core ($r \lesssim r_c$) that rotates rigidly, at a rate equal to that of the surface mid-latitudes;

3. A smooth matching of the core and envelope rotation profiles occurring across a thin spherical layer coinciding with the core-envelope interface ($r = r_c$), so that strong radial shears of opposite signs exist in the polar and equatorial regions.

Figure 7.6 shows the distribution of toroidal magnetic field (part B) resulting from the shearing of pure dipole with field strength $10^{-4}\,\mathrm{T}$ at $r/R = 0.7$ (part A, dotted lines) by the above solar-like differential rotation profile (part A, solid lines). This is nothing more that eq. (7.29) evaluated for $t = 10\,\mathrm{yr}$, with $B(r, \theta, 0) = 0$. Not surprisingly, the toroidal field is concentrated in the regions of large radial shear, at the core-envelope interface (dashed line). Note how the toroidal field distribution is *antisymmetric* about the equatorial plane, in agreement with Hale's polarity rules, and precisely what one would expect from the inductive action of a shear flow that is equatorially symmetric on a poloidal magnetic field that is itself antisymmetric about the equator.

Knowing the distributions of toroidal and poloidal fields on Figure 7.6 allows us to flirt a bit with dynamics, by computing the ϕ-component of the Lorentz force:

$$[\mathbf{F}_L]_\phi = \frac{1}{\mu_0 \varpi} \mathbf{B}_p \cdot \nabla(\varpi B) \ , \tag{7.32}$$

The resulting spatial distribution of $[\mathbf{F}_L]_\phi$ is plotted on Figure 7.6C. Examine Fig. 7.6 carefully to convince yourself that the Lorentz force is such as to *oppose* the driving shear. This is an important and totally general property of interacting flows and magnetic fields: the Lorentz force tends to resist the hydrodynamical stretching responsible for field induction. The ultimate

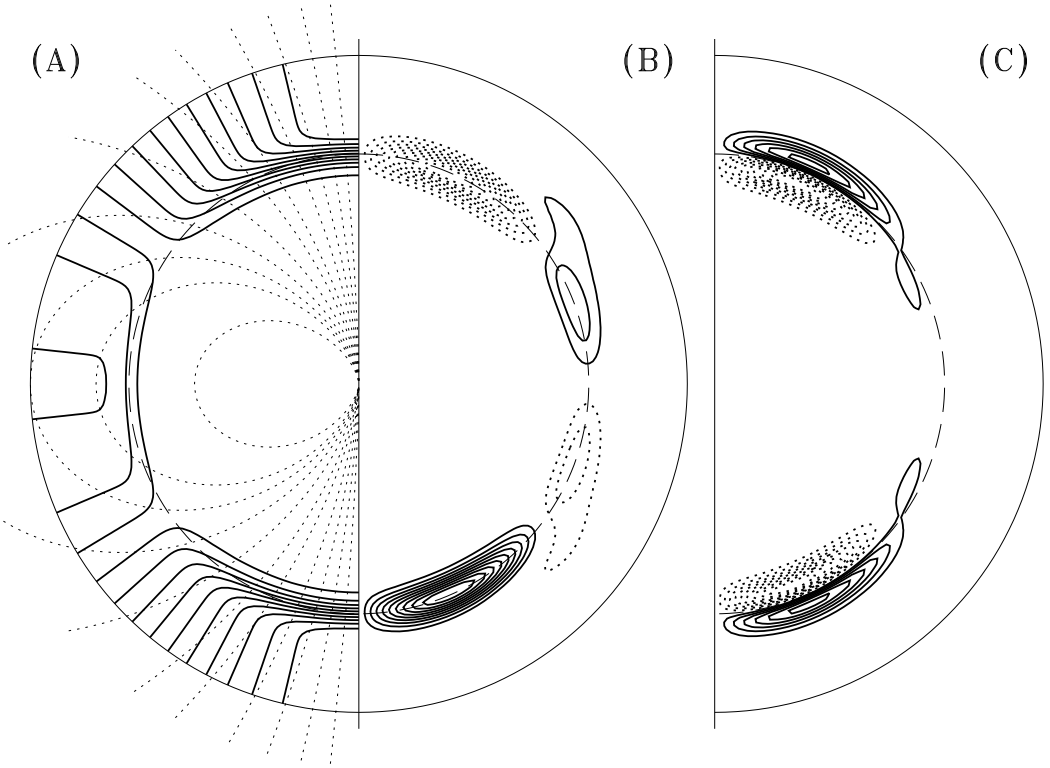

Figure 7.6: Shearing of a poloidal field into a toroidal component by a solar-like differential rotation profile. Part A shows isocontours of the rotation rate $\Omega(r,\theta)/2\pi$ (solid lines, contour spacing 10 nHz as on Fig. 7.5). The dotted lines are fieldlines for a pure dipole. The dashed line is the core-envelope interface at $r/R = 0.7$. Part B shows isocontours of the toroidal field, with solid (dotted) contours corresponding to positive (negative) B. The maximum toroidal field strength is about 0.2T, and contour spacing is 0.02T. Part C shows logarithmically spaced isocontours of the ϕ-component of the Lorentz force associated with the poloidal/toroidal fields of panels A and B.

fate of the system depends on whether the Lorentz force become dynamically significant before the growth of the toroidal field is mitigated by resistive dissipation; in the solar interior the former situation is far more likely[11].

Clearly, the growing magnetic energy of the toroidal field is supplied by the kinetic energy of the rotational shearing motion (this is hidden the second term on the RHS of eq. (1.87)). In the solar case, this is an attractive field amplification mechanism, because the available supply of rotational kinetic energy is immense. But don't make the mistake of thinking that this is a dynamo! In obtaining eq. (7.29) we have completely neglected magnetic dissipation, and remember, the dynamo we are seeking are flows that can amplify and sustain a magnetic field *against* Ohmic dissipation. Nonetheless, shearing of a poloidal field by differential rotation will turn out to be a central component of *all* solar/stellar dynamo models constructed in later chapters. It is also largely responsible for the strong alignement of galactic magnetic fields with the direction of galactic rotation, as evidence e.g. on Fig. 2.11.

7.3 Magnetic field evolution in a cellular flow

Having examined separately the resistive decay and hydrodynamical induction of magnetic field, we now turn to a situation where both processes operate simultaneously.

[11] How would you go about seeking a theoretical justification for this rather sweeping statement?

7.3.1 A cellular flow solution

In Cartesian geometry, we consider the action of a steady, incompressible ($\nabla \cdot \mathbf{u} = 0$) two-dimensional flow

$$\mathbf{u}(x,y) = u_x(x,y)\hat{\mathbf{e}}_x + u_y(x,y)\hat{\mathbf{e}}_y \tag{7.33}$$

on a two-dimensional magnetic field

$$\mathbf{B}(x,y,t) = B_x(x,y,t)\hat{\mathbf{e}}_x + B_y(x,y,t)\hat{\mathbf{e}}_y \ . \tag{7.34}$$

Note that neither the flow nor the magnetic field have a z-component, and that their x and y-components are both independent of the z-coordinate. The flow is said to be **planar** because $u_z = 0$, and has an ignorable coordinate (i.e., translational symmetry) since $\partial/\partial z \equiv 0$ for all field and flow components. Such a magnetic field can be represented by the vector potential

$$\mathbf{A} = A(x,y,t)\hat{\mathbf{e}}_z \ , \tag{7.35}$$

where, as usual, $\mathbf{B} = \nabla \times \mathbf{A}$. Under this representation, lines of constant A in the $[x,y]$ plane coincide with magnetic fieldlines. The only non-trivial component of the induction equation (1.105) is its z-components, which takes the form

$$\frac{\partial A}{\partial t} + \mathbf{u} \cdot \nabla A = \eta \nabla^2 A \ . \tag{7.36}$$

This is a linear advection-diffusion equation, describing the transport of a passive scalar quantity A by a flow $\mathbf{u}$, and subject to diffusion, the magnitude of which being measured by η. In view of the symmetry and planar nature of the flow, it is convenient to write the 2-D flow field in terms of a stream function $\Psi(x,y)$:

$$\mathbf{u}(x,y) = u_0 \left(\frac{\partial \Psi}{\partial y}\hat{\mathbf{e}}_x - \frac{\partial \Psi}{\partial x}\hat{\mathbf{e}}_y \right) \ . \tag{7.37}$$

It is easily verified that any flow so defined will identically satisfy the condition $\nabla \cdot \mathbf{u} = 0$. As with eq. (7.35), a given numerical value of Ψ uniquely labels one streamline of the flow. Consider now the stream function

$$\Psi(x,y) = \frac{L}{4\pi}\left(1 - \cos\left(\frac{2\pi x}{L}\right)\right)\left(1 - \cos\left(\frac{2\pi y}{L}\right)\right), \qquad x,y \in [0,L] \tag{7.38}$$

This describes a counterclockwise cellular flow centered on $(x,y) = (L/2, L/2)$, as shown on Figure 7.7. The maximal velocity amplitude $\max\|\mathbf{u}\| = u_0$ is found along the streamline $\Psi = u_0 L/(2\pi)$, plotted as a thicker line on Figure 7.7. This streamline is well approximated by a circle of radius $L/4$, and its streamwise circulation period turns out to be $1.065\pi L/2u_0$, quite close to what one would expect in the case of a perfectly circular streamline. In what follow this timescale is denoted τ_c and referred to as the **turnover time** of the flow. Note that both the normal and tangential components of the flow vanish on the boundaries $x = 0, L$ and $y = 0, L$. This implies that the domain boundary is itself a streamline ($\Psi = 0$, in fact), and that every streamline interior to the boundary closes upon itself within the spatial domain. These (simple) topological properties of the flow defined by eqs. (7.37) and (7.38) may seem largely irrelevant at this stage of our inquiries, but later chapters will reveal that they are in fact crucial to the dynamo problem.

We now investigate the inductive action of this flow by solving a nondimensional version of eq. (7.36), by expressing all lengths in units of L, and time in units of the **advection time** L/u_0, so that

$$\frac{\partial A}{\partial t} = -\frac{\partial \Psi}{\partial y}\frac{\partial A}{\partial x} + \frac{\partial \Psi}{\partial x}\frac{\partial A}{\partial y} + \frac{1}{\mathrm{R}_m}\left(\frac{\partial^2 A}{\partial x^2} + \frac{\partial^2 A}{\partial y^2}\right) \ , \qquad x,y \in [0,L] \ , \tag{7.39}$$

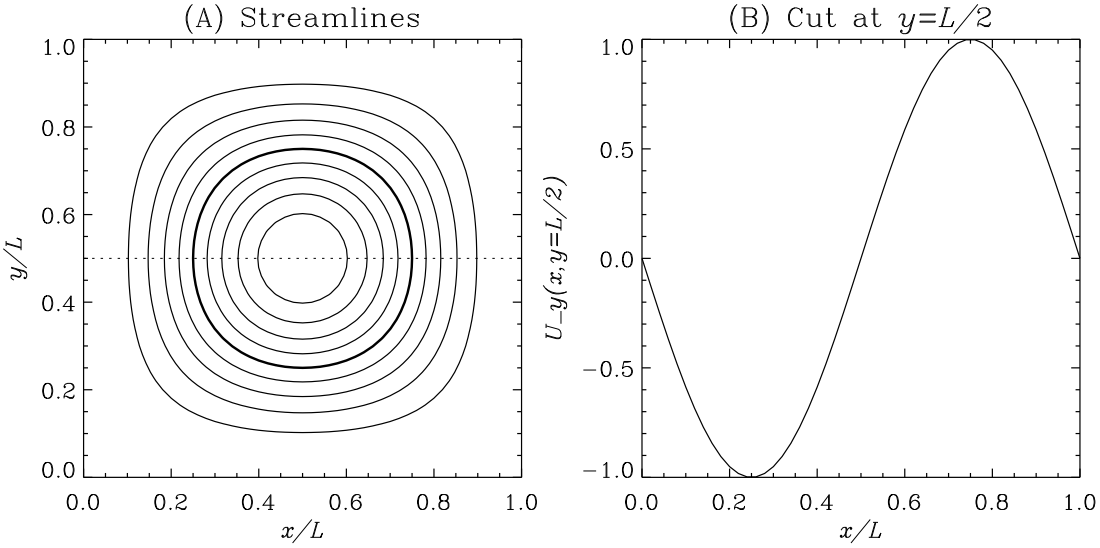

Figure 7.7: Counterclockwise cellular flow generated by the streamfunction given by eq. (7.38). Part (A) shows streamlines of the flow, with the thicker streamline corresponding to $\Psi = u_0 L/(2\pi)$, on which the flow attains its maximum speed u_0. Part (B) shows the profile of $u_y(x)$ along an horizontal cut at $y = 1/2$. A "typical" length scale for the flow is then $\sim L$.

where $\mathrm{R}_m = u_0 L/\eta$ is the magnetic Reynolds number for this problem, and the corresponding diffusion time is then $\tau_\eta = \mathrm{R}_m$ in dimensionless units. Equation (7.39) is solved as an initial-boundary value problem in two spatial dimensions, with spatial and temporal derivatives both evaluated using second-order centered finite differences (see Appendix F). All calculations described below start at $t = 0$ with an initially uniform, constant magnetic field $\mathbf{B} = B_0 \hat{\mathbf{e}}_x$, equivalent to:

$$A(x, y, 0) = B_0\, y \ . \tag{7.40}$$

We consider a situation where the magnetic field normal to the boundaries is held fixed, which amounts to holding the vector potential fixed on the boundary[12]. Figure 7.8 shows the variation with time of the magnetic energy (eq. (1.92)), for four solutions having $\mathrm{R}_m = 10, 10^2, 10^3$ and 10^4. Figure 7.9 shows the evolving shape of the magnetic fieldlines in the $\mathrm{R}_m = 10^3$ solution at 9 successive epochs[13]. The solid dots are "floaters", namely Lagrangian markers moving along with the flow. At $t = 0$ all floaters are equidistant and located on the fieldline initially coinciding with the coordinate line $y/L = 0.5$, that (evolving) fieldline being plotted in the same color as the floaters on all panels. Figure 7.9 covers two turnover times.

At first, the magnetic energy increases quadratically in time. This is precisely what one would expect from the shearing action of the flow on the initial B_x-directed magnetic field, which leads to a growth of the B_y-component that is linear in time. However, for $t/\tau_\mathrm{c} \gtrsim 2$ the magnetic energy starts to decrease again and eventually ($t/\tau_\mathrm{c} \gg 1$) levels off to a constant value. To understand the origin of this behavior we need to turn to Figure 7.9 and examine the solutions in some detail.

The counterclockwise shearing action of the flow is quite obvious on Fig. 7.9 in the early phases of the evolution, leading to a rather pretty spiral pattern as magnetic fieldlines get wrapped around one another. Note that the distortion of magnetic fieldlines by the flow implies a great deal of *stretching* in the streamwise direction. This is most obvious upon noting that the distance between adjacent floaters increases monotonically in time. It is no accident that the floaters end up in the regions of maximum field amplification on frames 2—5; they are

[12] Can you figure that one out?

[13] An animation of this evolving solution can be viewed on the course Web Page.

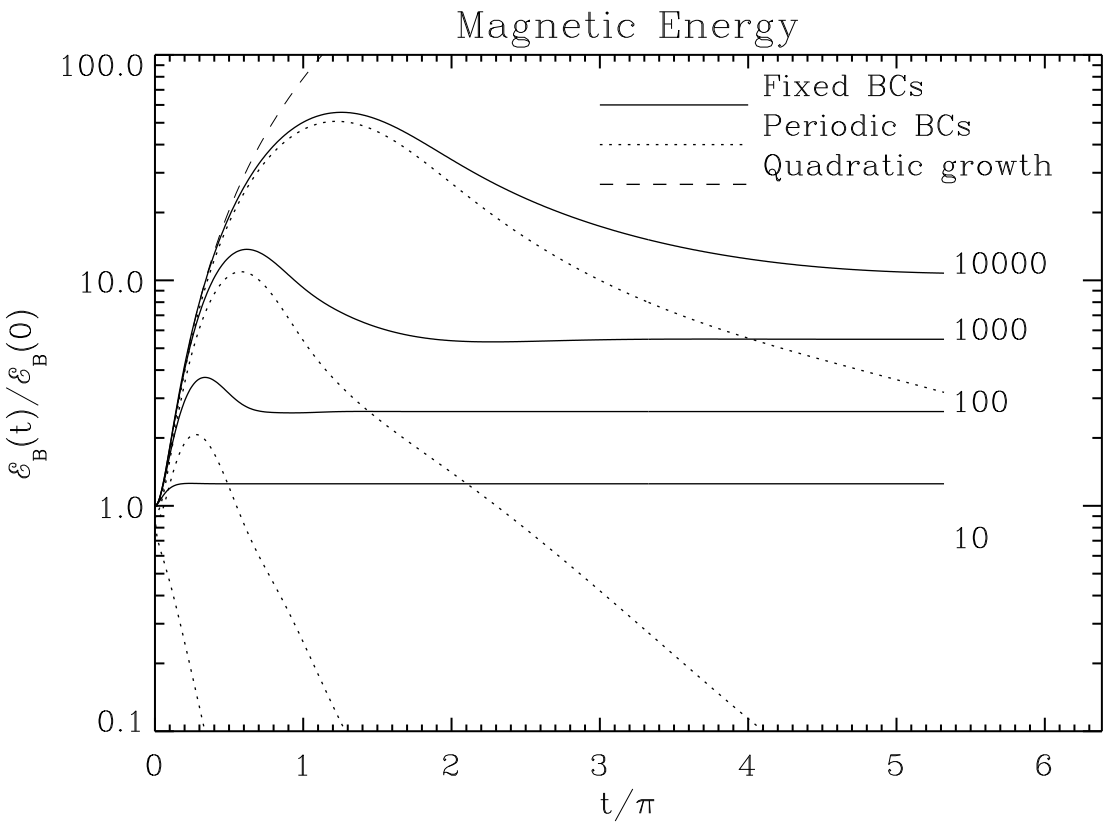

Figure 7.8: Evolution of the magnetic energy for solutions with increasing R_m. The solutions have been computed over 10 turnover times, at which point they are getting reasonably close to steady-state, at least as far as magnetic energy is concerned. One turnover time corresponds to $t/\pi = 0.532$.

initially positioned on the fieldline coinciding with the line $y = L/2$, everywhere perpendicular to the shearing flow (see Fig. 7.7), which pretty much ensures maximal inductive effect, as per eq. (7.36). The fact that all floaters remain at first "attached" onto their original fieldline is what one would have expected from the fact that this is a relatively high-R_m solution, so that flux-freezing is effectively enforced. As the evolution proceeds, the magnetic field keeps building up in strength (as indicated by the color scale), but is increasingly confined to spiral "sheets" of decreasing thickness.

By the time we hit one turnover time (corresponding approximately to frame 5 on Fig. 7.9), it seems that we are making progress towards our goal of producing a dynamo; we have a flow field which, upon acting on a preexisting magnetic field, has intensified the strength of that field, at least in some localized regions of the spatial domain. However, beyond $t \sim \tau_c$ the sheets of magnetic fields are gradually disappearing, first near the center of the flow cell (frames 5—7), and later everywhere except close to the domain boundaries (frames 7—9). Notice also how, from frame 5 onward, the floaters are seen to "slip" off their original fieldlines. This means that flux-freezing no longer holds; in other words, diffusion is taking place. Yet, we evidently still have $t \ll \tau_\eta$ ($\equiv R_m = 10^3$ here), which indicates that diffusion should not yet have had enough time to significantly affect the solution. What is going on here?

7.3.2 Flux expulsion

The solution to this apparent dilemma lies with the realization that we have defined R_m in terms of the global length scale L characterizing the flow. This was a perfectly sensible thing to

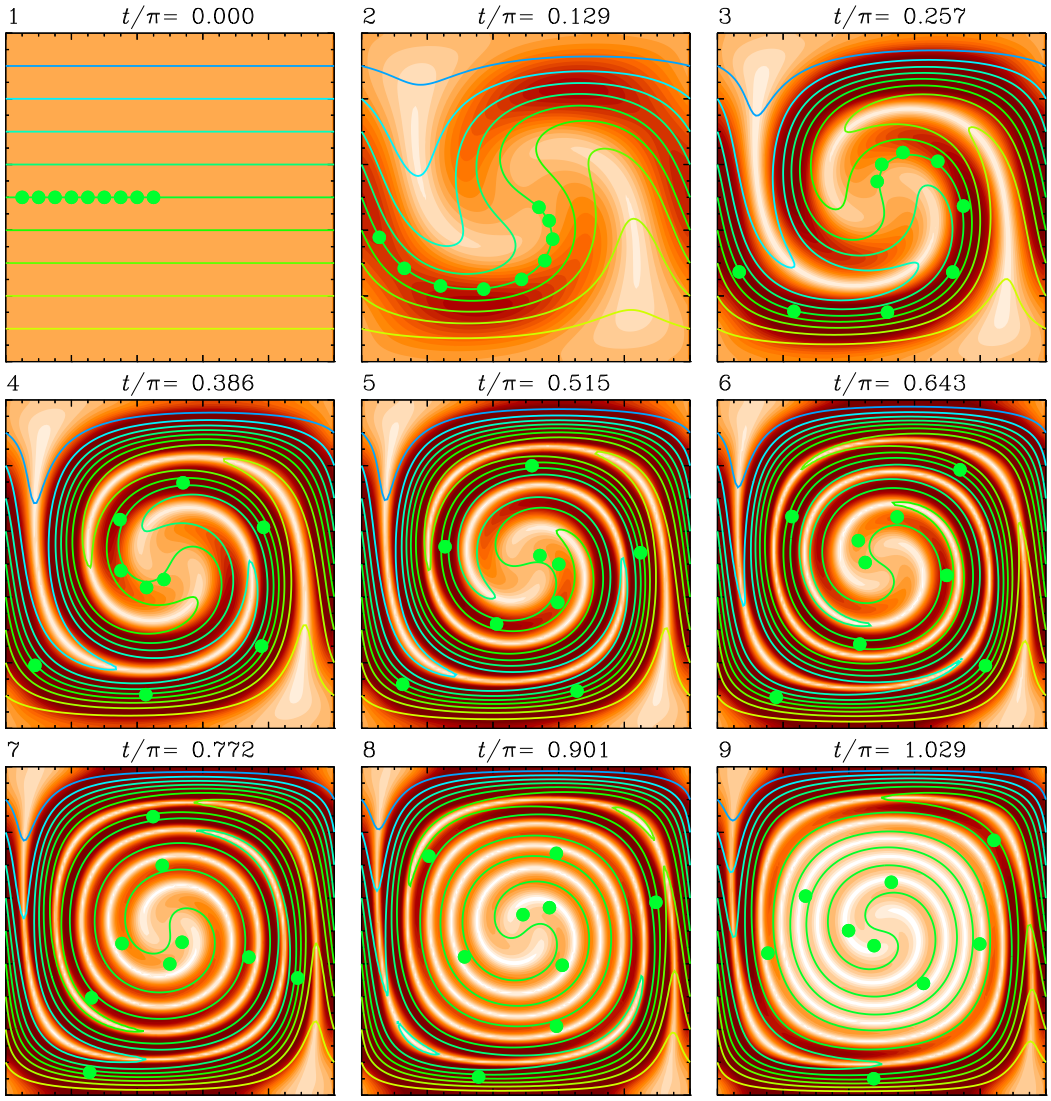

Figure 7.9: Solution to equation (7.39) starting from an initially horizontal magnetic field. The panels show the shape of the magnetic fieldlines at successive times. The color scale encodes the absolute strength of the magnetic field, i.e., $\sqrt{B_x^2 + B_y^2}$. The x- and y-axes are horizontal and vertical, respectively, and span the range $x, y \in [0, L]$. Time t is in units of L/u_0. The solid dots are "floaters", i.e., Lagrangian marker passively advected by the flow. The magnetic Reynolds number is $\mathrm{R}_m = 10^3$.

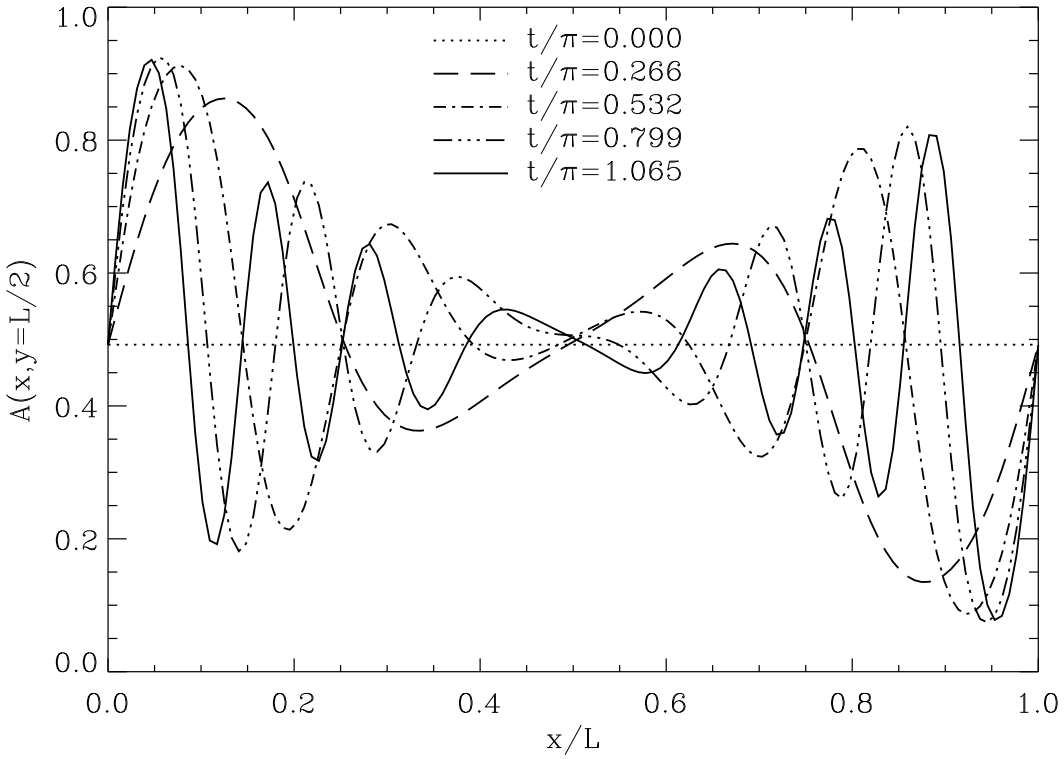

Figure 7.10: Cuts of a $\mathrm{R}_m = 10^4$ solution along the coordinate line $y = 0.5$, at successive times. Note how the "typical" length scale ℓ for the solution decreases with time, from $\ell/L \sim 0.25$ at $t/\pi = 0.269$, down to $\ell/L \sim 0.05$ after two turnover times ($t/\pi = 1.065$).

do on the basis of the flow configuration and initial condition on the magnetic field. However, as the evolution proceeds beyond $\sim \tau_\mathrm{c}$ the decreasing thickness of the magnetic field sheets means that the global length scale L is no longer an adequate measure of the "typical" length scale of the magnetic field, which is what is needed to estimate the diffusion time τ_η (see eq. (7.2)). Figure 7.10 shows a series of cuts of the vector potential A in a $\mathrm{R}_m = 10^4$ solution, plotted along the coordinate line $y = L/2$, at equally spaced successive time intervals covering two turnover times. Clearly the inexorable winding of the fieldline leads to a general decrease of the length scale characterizing the evolving solution. In fact, each turnover time adds two new "layers" of alternating magnetic polarity to the spiraling sheet configuration, so that the average length scale ℓ decreases as t^{-1}:

$$\frac{\ell(t)}{L} \propto \frac{L}{u_0 t} \ , \tag{7.41}$$

which in turn implies that the *local* dissipation time is also decreasing as t^{-1}. On the other hand, examination of Fig. 7.9 soon reveals that the (decreasing) length scale characterizes the thickness of elongated magnetic structures that are themselves more or less *aligned* with the streamlines, so that the turnover time τ_c remains the proper timescale measuring field induction. With τ_c fixed and τ_η inexorably decreasing, the solution is bound to reach a point where $\tau_\eta \simeq \tau_\mathrm{c}$, *no matter how small dissipation actually is*. To reach that stage just takes longer in the higher R_m solutions, since more winding of the fieldlines is needed. Larger magnetic energy can build up in the transient phase, but the growth of the magnetic field is *always* arrested. Equating τ_c ($\sim L/u_0$) to the *local* dissipation time ℓ^2/η, one readily finds that the length scale ℓ at which

both process become comparable can be expressed in terms of the *global* R_m as

$$\frac{\ell}{L} = (\mathrm{R}_m)^{-1/2} \ , \qquad \mathrm{R}_m = \frac{u_0 L}{\eta} \ . \tag{7.42}$$

That such a balance between induction and dissipation materializes means that a steady-state can be attained. Figure 7.11 shows four such steady states solutions for increasing values of the (global) magnetic Reynolds number R_m. The higher R_m solutions clearly show **flux expulsion** from the central regions of the domain. This is a general feature of steady, high-R_m magnetized flows with closed streamlines: magnetic flux is expelled from the regions of closed streamlines towards the edges of the flow cells, where it ends up concentrated in **boundary layers** which indeed have a thickness of order $\mathrm{R}_m^{-1/2}$, as suggested by eq. (7.42). It is important to understand how and why this happens.

To first get an intuitive feel for how flux expulsion operates, go back to Figure 7.9. As the flow wraps the fieldlines around one another, it does so in a manner that folds fieldlines of opposite polarity closer and closer to each other. When two such fieldlines are squeezed closer together than the dissipative length scale (eq. [7.42]), resistive decay takes over and destroys the field faster than it is being stretched. This is another instance of destructive folding, and can only be avoided along the boundaries, where the normal component of the field is held fixed. For flux expulsion to operate, flux-freezing must be effectively enforced on the spatial scale of the flow. Otherwise the field is largely insensitive to the flow, and fieldlines are hardly deformed with respect to their initial configuration (as on panel [A] of Fig. 7.11).

Consider now the implication for the total magnetic flux across the domain; flux conservation requires that the normal flux $B_0 L$ imposed at the right and left boundaries must somehow cross the interior, otherwise Maxwell's equation $\nabla \cdot \mathbf{B} = 0$ would not be satisfied; because of flux expulsion, it can only do so in the thin layers along the bottom and top boundaries. Since the thickness of these layers scales as $\mathrm{R}_m^{-1/2}$, it follows that the field strength therein scales as $\sqrt{\mathrm{R}_m}$, which in turn implies that the total magnetic energy in the domain also scales as $\sqrt{\mathrm{R}_m}$ in the $t \gg \tau_c$ limit [14].

7.3.3 Digression: the electromagnetic skin depth

You may recall that a sinusoidally oscillating magnetic field imposed at the boundary of a conductor will penetrate the conductor with an amplitude decreasing exponentionally away from the boundary and into the conductor, with a length scale called the **electromagnetic skin depth**:

$$\ell = \sqrt{\frac{2\eta}{\omega}} \ . \tag{7.43}$$

Now, go back to the cellular flow and imagine that you are an observer located in the center of the flow cell, looking at the domain boundaries while rotating with angular velocity u_0/L; what you "see" in front of you is an "oscillating" magnetic field, in the sense that it flips sign with "angular frequency" u_0/L. The corresponding electromagnetic skin depth would then be

$$\frac{\ell}{L} = \sqrt{\frac{2\eta}{u_0 L}} =\equiv \sqrt{\frac{2}{\mathrm{R}_m}} \ . \tag{7.44}$$

which basically corresponds to the thickness of the boundary layer where significant magnetic field is present in the steady-states shown on Figure 7.11. How about that for a mind flip...

7.3.4 Timescales for field amplification and decay

Back to our cellular flow. Flux expulsion or not, it is clear from Figure 7.8 (solid lines) that some level of field amplification has occurred in the high R_m solutions, in the sense that $\mathcal{E}_B(t \rightarrow$

[14] Hold it, $\mathcal{E}_\mathrm{B} \propto \mathbf{B}^2$ as per eq. (1.92); how can the magnetic field strength and magnetic energy *both* scale as $\sqrt{\mathrm{R}_m}$?

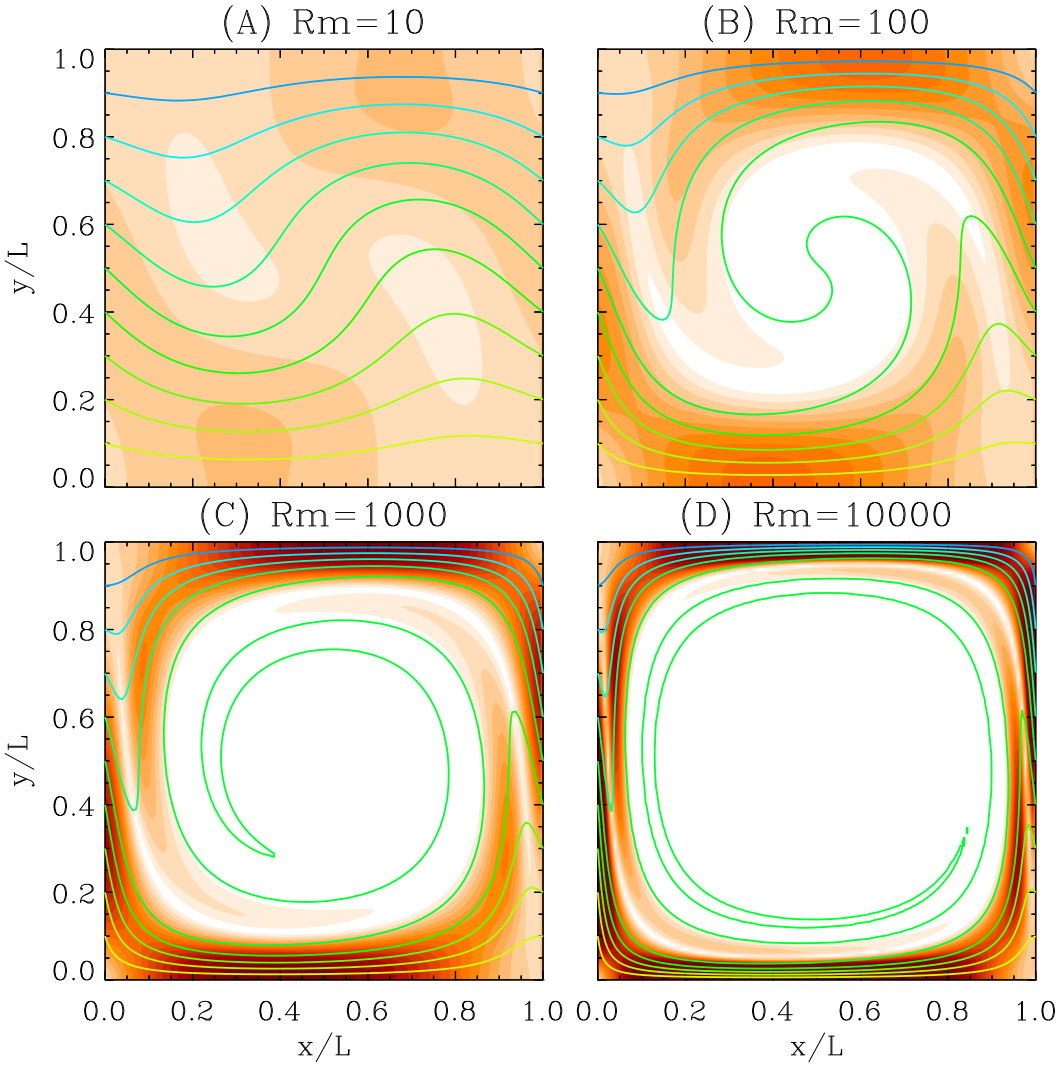

Figure 7.11: Steady-state solutions to the cellular flow problem, for increasing values of the magnetic Reynolds number R_m. The $R_m = 10^4$ solution is at the resolution limit of the $N_x \times N_y = 128 \times 128$ mesh used to obtain these solutions, as evidenced on part (D) by the presence of small scale irregularities where magnetic fieldlines are sharply bent. The color scale encodes the local magnitude of the magnetic field. Note how, in the higher R_m solutions, magnetic flux is expelled from the center of the flow cell. With $\mathcal{E}_B(0)$ denoting the energy of a purely horizontal field with same normal boundary flux distribution, the magnetic energy for these steady states is $\mathcal{E}_B/\mathcal{E}_B(0) = 1.37$, 2.80, 5.81 and 11.75, respectively, for panels (A) through (D).

$\infty) > \mathcal{E}_B(0)$. But is this a dynamo? The solutions of Fig. 7.11 have strong electric currents in the direction perpendicular to the plane of the paper, and these currents are subjected to resistive dissipation. Have we then reached the goal stated at the beginning of the chapter, namely, to amplify and maintain a weak, preexisting magnetic field against Ohmic dissipation?

In a narrow sense yes, but a bit of reflection will show that the boundary conditions are playing a crucial role. The only reason that the magnetic energy does not asymptotically go to zero is that the normal field component is held fixed at the boundaries, which, in the steady-state, implies a non-zero Poynting flux into the domain across the left and right vertical boundaries. The magnetic field is not avoiding resistive decay because of field induction within the domain, but rather because external energy (and magnetic flux) is being pumped in through the boundaries. This is precisely what is embodied in the second and third terms on the RHS of eq. (1.87).

What if this were not the case? One way to work around the boundary problem is to replace the fixed flux boundary conditions by periodic boundary conditions:

$$A(x,0) = A(x,L) \ , \qquad A(0,y) = A(L,y) \ . \tag{7.45}$$

There is still a net flux across the vertical boundary at $t = 0$, but the boundary flux is now free to decay away along with the solution. You get to compute such a solution in Problem 7.5 It is time to reveal that the hitherto unexplained dotted lines on Fig. 7.8 correspond in fact to solutions computed with such boundary conditions, for the same cellular flow and initial condition as before.

Evidently the magnetic energy now decays to zero, confirming that the boundaries indeed played a crucial role in the sustenance of the magnetic field in our previous solutions. What is noteworthy is the rate at which it does so. In the absence of the flow and with freely decaying boundary flux, the initial field would diffuse away on a timescale $\tau_\eta \sim L^2/\eta$, which is equal to R_m if we retain the scaling of τ in terms of L/u_0. With the flow turned on, the decay proceeds at an accelerated rate because of the inexorable decrease of the typical length scale associated with the evolving solution, which we argued earlier varied as t^{-1}. What then is the typical timescale for this enhanced dissipation? The decay phase of the field (for $t \gg L/u_0$) is approximately described by

$$\frac{\partial A}{\partial t} = \eta \nabla^2 A \ . \tag{7.46}$$

An estimate for the dissipation timescale can be obtained once again via dimensional analysis, by replacing ∇^2 by $1/\ell^2$, as in §7.1 but now with the important difference that ℓ is now a function of time:

$$\ell \to \ell(t) = \left(\frac{L}{t}\right)\left(\frac{L}{u_0}\right) \ , \tag{7.47}$$

in view of our previous discussion (cf. Fig. 7.10 and accompanying text). This leads to

$$\frac{\partial A}{\partial t} \simeq -\frac{\eta u_0^2 t^2}{L^4} A \ , \tag{7.48}$$

where the minus sign is introduced in view of the fact that $\nabla^2 A < 0$ in the decay phase. Equation (7.48) integrates to

$$\frac{A(t)}{A_0} = \exp\left[-\frac{\eta u_0^2}{3L^4} t^3\right] = \exp\left[-\frac{1}{3\mathrm{R}_m}\left(\frac{u_0^3 t^3}{L^3}\right)\right] \ . \tag{7.49}$$

This last expression indicates that with t measured in units of L/u_0, the decay time scales as $\mathrm{R}_m^{1/3}$. This is indeed a remarkable situation: in the low magnetic diffusivity regime (i.e., high R_m), the flow has in fact *accelerated* the decay of the magnetic field, even though large field

intensification can occur in the early, transient phases of the evolution. This is not at all what a dynamo should be doing!

As it turns out, flux expulsion is even trickier than the foregoing discussion may have led you to believe! Flux expulsion destroys the mean magnetic field component directed *perpendicular* to the flow streamlines. It cannot do a thing to a mean component oriented *parallel* to streamlines. For completely general flow patterns and initial conditions, the dissipative phase with timescale $\propto \mathrm{R}_m^{1/3}$ actually characterizes the approach to a state where the advected trace quantity —here the vector potential A— becomes constant *along each streamline*, at a value $\bar{A}$ equal to the initial value of A averaged on each of those streamlines. For the cellular flow and initial conditions used above, this average turns out to be $\bar{A} = 0.5$ *for every streamline*, so that the $\mathrm{R}_m^{1/3}$ decay phase corresponds to the true decay of the magnetic field to zero amplitude. If $\bar{A}$ varies from one fieldline to the next, however, the $\mathrm{R}_m^{1/3}$ phase is followed by a third decay phase, which proceeds on a timescale $\sim \mathrm{R}_m$, since induction no longer operates ($\mathbf{u} \cdot \nabla A = 0$) and the typical length scale for A is once again L. You get to explore this phenomenon in problem 7.6 [15]. At any rate, even with a more favorable initial condition we have further delayed field dissipation, but we still don't have a dynamo since dissipation will proceed inexorably, on the "long" timescale $\mathrm{R}_m(L/u_0)$.

7.3.5 Global flux expulsion in spherical geometry: axisymmetrization

You may think that the flux expulsion problem considered in the preceding section has nothing to do with any astronomical objects you are likely to encounter in your future astrophysical carreers. Wroooong!

Consider the evolution of a magnetic field pervading a sphere of electrically conducting fluid, with the solar-like differential rotation profile already encountered previously (§7.2.3, Fig. 7.5 and eqs. (7.30)—(7.31)), and with the field having initially the form of an dipole whose axis is inclined by an angle Θ with respect to the rotation axis ($\theta = 0$). Such a magnetic field can be expressed in terms of a vector potential having components:

$$A_r(r, \theta, \phi) = 0 \tag{7.50}$$

$$A_\theta(r, \theta, \phi) = (R/r)^2 \sin\Theta(\sin\beta\cos\phi - \cos\beta\sin\phi) \tag{7.51}$$

$$A_\phi(r, \theta, \phi) = (R/r)^2[\cos\Theta\sin\theta - \sin\Theta\cos\theta(\cos\beta\cos\phi + \sin\beta\sin\phi)] \tag{7.52}$$

where β is the angle between the $\phi = 0$ plane, and the plane defined by the dipole and coordinate axes.

Now, the vector potential for an inclined dipole can be written as the sum of two contributions, the first corresponding to an aligned dipole ($\Theta = 0$), the second to a perpendicular dipole ($\Theta = \pi/2$), their relative magnitude being equal to $\tan\Theta$[16]. Since the governing equation is linear, the solution for an inclined dipole can be broken into two independent solutions for the aligned and perpendicular dipoles. The former is precisely what we investigated already in §7.2.3, where we concluded there that the shearing of an aligned dipole by an axisymmetric differential rotation would lead to the buildup of a toroidal component, whose magnitude would grow linearly in time at a rate set by the magnitude of the shear.

The solution for a perpendicular dipole is in many way similar to the cellular flow problem of §7.3. You can see how this may be the case by imagining looking from above onto the equatorial plane of the sphere; the fieldlines contained in that plane will have a curvature and will be contained within a circular boundary, yet topologically the situation is similar to the cellular flow studied in the preceding section: the (sheared) flow in the equatorial plane is made

[15] In case you're too lazy to do the problem, you can view an animation of this solution on the Course Home Page. But please do the problem anyway.

[16] Can you work out the corresponding vector potential components ?

of closed, circular streamlines contained within that plane, so that we can expect flux expulsion to occur. The equivalent of the turnover time here is the differential rotation timescale, namely the time for a point located on the equator to perform a full 2π revolution with respect the poles:

$$\tau_{\rm DR} = (\Omega_{\rm Equ} - \Omega_{\rm Pole})^{-1} = \Omega_\odot (a_2 + a_4) \ , \tag{7.53}$$

where the second equality follows directly from eq. (7.31). For a freely decaying dipole, the perpendicular component of the initial dipole will then be subjected to flux expulsion, and dissipated away, at a rate far exceeding purely diffusive decay in the high R_m limit, as argued earlier.

But here is the amusing thing; for an observer looking at the magnetic field at the surface of the sphere, the enhanced decay of the perpendicular component of the dipole will translate into a gradual decrease in the inferred tilt axis of the dipole. Figure 7.12 shows this effect, for the differential rotation profile given by eq. (7.30) and a magnetic Reynolds number $R_m = 10^3$. Contours of constant B_r are plotted on the surface $r/R = 1$, with the neutral line ($B_r = 0$) plotted as a thicker line. At $t = 0$ the field has the form of a pure dipole tilted by $\pi/3$ with respect to the coordinate axis, and the sphere is oriented so that the observer (you!) is initially looking straight down the magnetic axis of the dipole. Advection by the flow leads to a distorsion of the initial field, with the subsequent buildup of small spatial scales in the r- and $\theta-$directions (only the latter can be seen here)[17]. After two turnover times (last frame), the surface field looks highly axisymmetric.

So, in a differentially rotating fluid system with high R_m, flux expulsion leads to the **symmetrization** of any non-axisymmetric magnetic field component initially present —or contemporaneously generated. The efficiency of the symmetrization process should make us a little cautious in assuming that the large-scale magnetic field of the Sun, which one would deem roughly axisymmetric upon consideration of surface things like the sunspot butterfly diagram, is characterized by the same level of axisymmetry in the deep-seated generating layers, where the dynamo is presumed to operate. After all, standing in between is a thick, axisymmetrically differentially rotating convective envelope that must be reckoned with. In fact, observations of coronal density structures in the descending phase of the solar cycle can be interpreted in terms of a large-scale, tilted dipole component, with the tilt angle steadily decreasing over 3—4 years towards solar minimum. Interestingly, the differential rotation timescale for the Sun is ~ 6 months. Are we seeing the axisymmetrization process in operation ? Maybe. Axisymmetry is certainly a very convenient modeling assumption when working on the large scales of the solar magnetic field, but it may be totally wrong.

You may recall from §2.2 that the magnetic field of Saturn stands out among other solar system planets as having a symmetry axis aligned exactly with its rotation axis. Saturn also has the strongest large-scale surface differential rotation, with a broad equatorial "jet" peaking at $\sim$ 5 times the polar angular velocity. Structural models of Saturn also indicate that this differential rotation may well extend in the interior, with the angular velocity being constant along cylinders concentric with the rotation axis. Saturn's magnetic field is most likely generated by a dynamo mechanism operating in its metallic Hydrogen core, extending to a fractional radius of about 0.55. So imagine now that the dynamo-generated field is indeed inclined with respect to the rotation axis, like in most other planets. In between this field and the surface, where we make measurement, there stands a strongly differentially rotating partly conducting envelope, where axisymmetrization can take place. The key here is that the electrical conductivity in the molecular Hydrogen envelope must be sufficiently large for a coupling between the flow and field (in other words, we need $\mathrm{R}_m \gtrsim 1$, not $\mathrm{R}_m \ll 1$. See the references listed in the bibliography for more on this interesting Saturnian problem.

[17] An animation of this solution, as well as a few others for different R_m and/or tilt angle, can be viewed on the course Web Page.

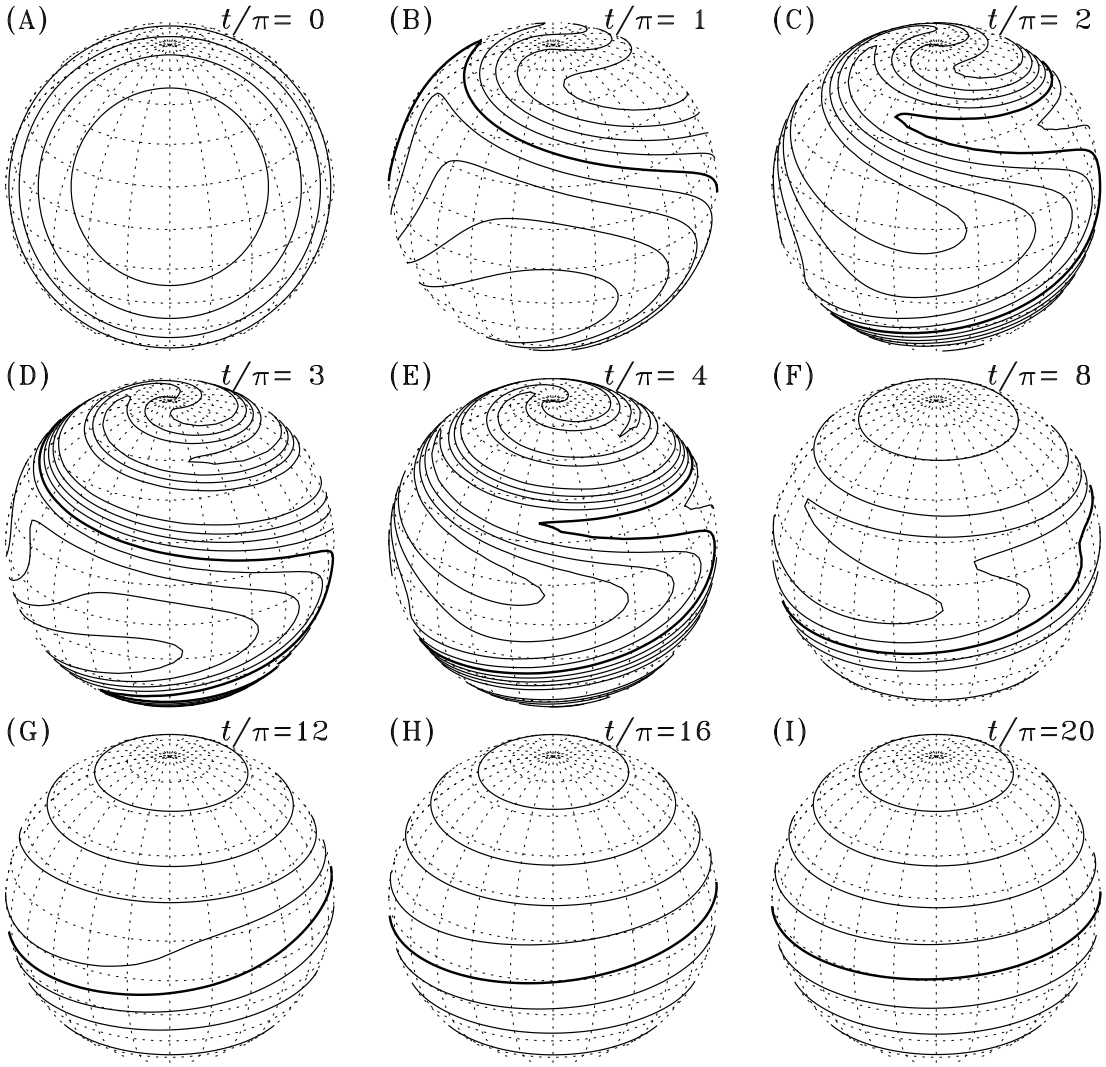

Figure 7.12: Symmetrization of an inclined dipole in a electrically conducting sphere in a state of solar-like axisymmetric differential rotation. Each panel shows contours of constant B_r at the surface of the sphere, and the solution is matched to a potential in the exterior ($r/R > 1$). The differential rotation is given by eq. (7.30). Time is given in units of $\tau_{\rm DR}$, in which the turnover period (or differential rotation period) is equal to 2π.

7.4 Two anti-dynamo theorems

The cellular flow studied in §7.3, although it initially looked encouraging (cf. Fig. 7.8), proved not to be a dynamo after all. Is this peculiar to the flow defined by eqs. (7.37)–(7.38), or is this something more general? Exhaustively testing for dynamo action in all possible kinds of flow geometries is clearly impractical. However, it turns out that one can rule out *a priori* dynamo action in many classes of flows. These demonstrations are known as **anti-dynamo theorems**.

A powerful anti-dynamo theorem due to Ya. B. Zeldovich (1914-87), has a lot to teach us about our cellular flow results. The theorem rules out dynamo action in steady planar flows in cartesian geometry, i.e., flows of the form

$$\mathbf{u}_2(x,y,z) = u_x(x,y,z)\hat{\mathbf{e}}_x + u_y(x,y,z)\hat{\mathbf{e}}_y \tag{7.54}$$

in a bounded volume V at the boundaries (∂V) of which the magnetic field vanishes. Note that no other restrictions are placed on the magnetic field, which can depend on all three spatial coordinate as well as time. Nonetheless, in view of eq. (7.54) is will prove useful to consider separately the z-component of the magnetic field $B_z(x,y,z,t)$ from the (2D) field component in the $[x,y]$ plane (hereafter denoted $\mathbf{B}_2$). It is readily shown that the z-component of the induction equation then reduces to

$$\frac{\partial B_z}{\partial t} + \mathbf{u}\cdot\nabla B_z = \eta\nabla^2 B_z \tag{7.55}$$

for spatially constant magnetic diffusivity. Now, the LHS is just a Lagrangian derivative, yielding the time variation of B_z as one moves along with the fluid. Multiplying this equation by B_z and integrating over V yields, after judicious use of a suitable vector identity and of the divergence theorem[18]:

$$\frac{1}{2}\int_V \frac{\mathrm{D}B_z^2}{\mathrm{D}t}dV = \int_{\partial V} B_z(\nabla B_z)\cdot\mathbf{n}\mathrm{d}S - \eta\int_V (\nabla B_z)^2\mathrm{d}V \ . \tag{7.56}$$

Now, the first integral on the RHS vanishes since $\mathbf{B} = 0$ on ∂V by assumption. The second integral is positive definite, *therefore B_z always decays on the diffusive timescale* (cf. §7.1).

Consider now the magnetic field $\mathbf{B}_2$ in $[x,y]$ planes. The most general such 2D field can be written as the sum of a solenoidal and potential component:

$$\mathbf{B}_2(x,y,z,t) = \nabla\times(A\hat{\mathbf{e}}_z) + \nabla\Phi \ , \tag{7.57}$$

where the vector potential A and scalar potential Φ both depend on all three spatial coordinates and time. Evidently, the constraint $\nabla\cdot\mathbf{B} = 0$ implies

$$\nabla_2^2\Phi = -\frac{\partial B_z}{\partial z} \ , \tag{7.58}$$

where $\nabla_2^2 \equiv \partial^2/\partial x^2 + \partial^2/\partial y^2$ is the 2D Laplacian operator in the $[x,y]$ plane. Clearly, once B_z has resistively dissipated, i.e., for times much larger than the global resistive decay time τ, Φ is simply a solution of the 2D Laplace equation $\nabla_2^2\Phi = 0$.

Here comes the sneaky part. We take the curl of the induction equation. Upon substituting eq. (7.57), the z-component of the resulting expression yields

$$\nabla\times\nabla\times\left[\frac{\partial A}{\partial t} + \mathbf{u}_2\cdot\nabla A - \eta\nabla_2^2 A - \mathbf{u}_2\times\nabla\Phi\right] = 0 \ , \tag{7.59}$$

with $\nabla\cdot(A\hat{\mathbf{e}}_z) = 0$ as a choice of gauge. Note that only one term involving Φ survives, because $\nabla\times\nabla\Phi = 0$ identically. In general, the above expression is only satisfied if the quantity in square brackets itself vanishes, i.e.,

$$\frac{\mathrm{D}A}{\mathrm{D}t} = \eta\nabla_2^2 A + \mathbf{u}_2\times\nabla\Phi \ . \tag{7.60}$$

[18] Try it!

This expression is identical to that obtained above for B_z, except for the presence of the source term $\mathbf{u}_2 \times \nabla\Phi$. However, we just argued that for $t \gg \tau$, $\nabla_2^2\Phi = 0$. In addition, $\mathbf{B}$ vanishes on ∂V by assumption, so that the only possible asymptotic interior solutions are of the form $\Phi =$const, which means that the source term vanishes in the limit $t \gg \tau$. From this point on eq. (7.60) is indeed identical to eq. (7.55), for which we already demonstrated the inevitability of resistive decay. Therefore, dynamo action, i.e., maintenance of a magnetic field against resistive dissipation, is impossible in a planar flow for *any* 3D magnetic field.

Another powerful anti-dynamo theorem, predating in fact Zeldovich's, is due to T.G. Cowling (1906-90). This anti-dynamo theorem is particularly important historically, since it rules out dynamo action for 3D but axisymmetric flows and magnetic fields, which happen to be the types of flows and fields one sees in the Sun, at least on the larger spatial scales. Rather than going over one of the many very mathematical proofs of Cowling's theorem found in the literature, let's just follow the underlying logic of our proof of Zeldovich's theorem. Assuming once again that there are no sources of magnetic field exterior to the domain boundaries, we consider the inductive action of a 3D, steady axisymmetric flow on a 3D axisymmetric magnetic field. Recall from §1.12.3 that under these circumstances the induction equation can be separated into the two components given by eqs. (1.108)–(1.109). The LHS of these expressions is again a Lagrangian derivative for the quantities in parentheses, and the first terms on each RHS are of course diffusion. The next term on the RHS of eq. (1.109) vanishes for incompressible flows, and remains negligible for very subsonic compressible flows. The last term on the RHS, however, is a source term, in that it can lead to the growth of B *as long as* A *does not decay away.* This is the very situation we have considered in §7.2.3, by holding A fixed as per eq. (7.27). However, there is no similar source-like term on the RHS of eq. (1.108), which governs the evolution of A.

This should now start to remind you of Zeldovich's theorem. In fact, eq. (1.108) is structurally identical to eq. (7.55), for which we demonstrated the inevitability of resistive decay in the absence of sources exterior to the domain. This means that A will inexorably decay, implying in turn that B will then also decay once A has vanished. Since axisymmetric flows cannot maintain A against Ohmic dissipation, *a 3D axisymmetric flow cannot act as a dynamo for a 3D axisymmetric magnetic field.* [19]. Cowling's theorem is not restricted to spherical geometry, and is readily generalized to any situation where both flow and field showing translational symmetry in one and the same spatial coordinate. Such physical systems are said to have an **ignorable coordinate**.

It is worth pausing and reflecting on what these two antidynamo theorems imply for the cellular flow of §7.3. It was indeed a planar flow ($u_z = 0$), and moreover the magnetic field had an ignorable coordinate ($\partial\mathbf{B}/\partial z \equiv 0$)! We thus fell under the purview of both Zeldovich's and Cowling's theorems, so in retrospect our failure to find dynamo action is now understood. Clearly, the way to evade both theorems is to consider flows and fields that are fully three-dimensional, and lack translational symmetry at least in the magnetic field. This is precisely what we do in the following chapter.

Problems:

1. In this problem you get to do analytically the diffusion of toroidal field, which was only outlined in §7.1.3. Consider a constant-diffusivity sphere of radius R, and use our mixed "$A + B$" representation for an axisymmetric magnetic field (§1.12.3),

   (a) Starting from the MHD induction equation with $\mathbf{u} = 0$, obtain a diffusion-like equation for the toroidal component B.

[19] A fact often unappreciated is that Cowling's theorem does not rule out the dynamo generation of a *non-axisymmetric* 3D magnetic field by a 3D axisymmetric flow.

(b) Assuming now that B can be expressed as

$$B(r,\theta,t) = \sum b_l f_l(r) P_l^0(\cos\theta)\exp(i\omega t) \ ,$$

obtain an eigenvalue equation for $f_l(r)$.

(c) Setting $B = 0$ at $r = R$, pull out out your handbook of special functions and verify that the eigenvalues given in §7.1.3 are indeed the correct ones.

2. This problems gets you to further explore the diffusive decay problem of §7.1.4 as a numerical 1-D eigenvalue problem. Use the same magnetic diffusivity profile (with $\Delta\eta = 10^{-2}$), but to avoid having to deal with the matching of your solutions to a potential field in $r/R > 1$, focus instead on the decay of purely *toroidal* axisymmetric magnetic fields. You may use the computing language of your choice, but please do include listings of all your codes with your solutions. Some useful Fortran-77 routines for the solution of tridiagonal systems of linear algebraic equations, together with instructions for use, can be obtained from the course Web Page:

`http://www.astro.umontreal.ca/~paulchar/phy6795/phy6795.html`

From the top of the main page, click on *Problems: Software and hints*, locate the appropriate subsection, and follow the instructions given there.

(a) By assuming a spatial dependence of the form given by eq. (7.12), show that eq. (7.1) reduces to eq. (7.13).

(b) Use centered finite differences to discretize eq. (7.13), and solve the resulting system of algebraic equations using inverse iteration. As a test of your numerical implementation, do first a problem for constant η, and compare your numerical results to the analytic solutions found in §7.1.3.

(c) Using now the error function profile for the magnetic diffusivity, obtain solutions for the first three angular degrees l and radial harmonics degrees n (for a total of 9 modes). Labels your solutions in terms of (l, n) values, and rank them according to decay time.

(d) Compare the decay times of your toroidal eigenmodes to those of poloidal eigenmodes of corresponding angular and radial degrees, as shown on Fig. 7.1. Can you pick out a trend ? If so, try to come up with a sensible explanation for it.

3. Go back to the case of shearing of a pure dipole by a parametrized solar-like differential rotation (§7.2.3);

(a) Starting from a poloidal field strength of 10^{-4} T at the core-envelope interface, calculate/estimate the time taken for the toroidal field strength to reach a strength of 1 T;

(b) By judicious dimensional analysis of the ϕ-component of the inviscid form of of the momentum equation, evaluate the timescale over which the rotational shear at the core-envelope interface would be altered by the Lorentz force, once the toroidal field strength has reached 1T;

(c) Is your result in (b) much longer or shorter than the solar cycle period? What does this suggest?

4. Fill in the missing mathematical steps leading to eq. (7.56).

5. Recompute the cellular flow solution of §7.3 using periodic boundary conditions. Use second order centered finite differences to discretize the RHS of eq. (7.39), and the leapfrog scheme for time stepping. Make use of the ghost cell formalism to enforce your periodic boundary conditions. Compute a $\mathrm{R}_m = 10^3$ solution using the initial condition given by eq. (7.40) compute the time evolution of the total magnetic energy, and verify that it matches that plotted on Fig. 7.8.

6. Repeat the calculation of the preceding problem (again with periodic boundary conditions), but now use this time as an initial condition a vector potential $A(y)$ that is gaussian in y and peaks at $y/L = 0.5$:

$$A(x, y, 0) = 2B_0 \exp\left(-\frac{(y - L/2)^2}{(L/4)^2}\right).$$

Compare the resulting magnetic energy evolution to that you obtained in problem 7.5, and search your second solution for evidence of three more or less distinct amplification and decay phases:

(a) Growth of the field, on timescale $\sim L/u_0$;

(b) Enhanced resistive decay, on a timescale $\sim \mathrm{R}_m^{1/3} \equiv 10(L/u_0)$;

(c) A final decay phase, with timescale $\sim \mathrm{R}_m \equiv 10^3(L/u_0)$;

7. There exist another, dynamical way to produce inexorably decreasing lengths scales in a MHD system, known as **phase mixing**. Consider an imcompressible, inviscid, perfectly conducting fluid contained between two infinite parallel plates located at $z = \pm L$, across which a magnetic field is imposed. This magnetic field is oriented vertically, but its strength increases with the y-direction, i.e., $\mathbf{B} = (0, 0, B_z(y))$. At $t = 0$, a shear in the x-direction is imposed on this reference state, i.e., $\mathbf{u} = (u_x(z), 0, 0)$, with $u_x(\pm L) = 0$ to satisfy the no-slip boundary conditions.

(a) Show that the x-components of the momentum and induction equations can be combined into a single wave-type equation for either B_x or u_x.

(b) Show that, in view of the boundary conditions on $\mathbf{u}$, this wave equation admits general solutions of the form

$$B_x(y, z, t) = \sum_{n=1}^{\infty} B_{n0} \cos\left(\frac{n\pi z}{2L}\right) \exp(-i\omega t) \ ,$$

where $\omega = u_A(y)/L$, with u_A the Alfvén speed along the vertical fieldline originally located at y, and with the numerical coefficients B_{n0} set by the initial condition.

(c) Assume now that $B_z \propto (1 + y)^2$, $y \in [0.1]$, and that only the fundamental ($n = 1$) mode is excited at $t = 0$; plot $B_x(y, z = 0)$ for constant time increments (use the inverse Alfvén frequency as a unit of time).

(d) Now Fourier transform the profiles you plotted, and verify that the power spectrum peaks at increasingly small wavelengths as time proceeds. Plot the wavenumber k_m corresponding to the peak in the power spectrum as a function of time, and estimate the time required for $k_m \to \infty$. Is the singularity reached in a finite time?

Bibliography:

The first detailed discussions of the diffusive decay of large-scale magnetic fields in astrophysical bodies are due to

Cowling, T.S. 1945, *Mon. Not. Roy. Astron. Soc.*, **105**, 166,
Wrubel, M.H. 1952, *Astrophys. J.*, **16**, 291.

On the numerical solution of algebraic eigenvalue problems in general, and on inverse iteration in particular, see

Golub, G.H., & Van Loan, C.F. 1989, *Matrix Computations (second edition)*, Baltimore: The Johns Hopkins University Press; §7.6.1 and 7.7.8.

Press, W.H., Teukolsky, S.A., Vetterling, W.T., & Flannery, B.P. 1992, *Numerical Recipes*, Second Ed., (Cambridge: Cambridge University Press), §11.7.

Chapter 11 of Press *et al.* also discusses numerical techniques that allow the computation of *all* eigenvalues of a matrix system, if you're interested in that. The book also contains a good introduction to the art of PDE discretization by finite differences. You will also find there a description of the leapfrog scheme for temporal dizcretisation. Among the numerous books discussing the calculation of macroscopic transport coefficients such as viscosity and electrical conductivity, starting from a microscopic point of view, our preference goes to an old classic:

Spitzer, L. Jr. 1962, *Physics of Fully Ionized Gases* (second ed.), New York: Wiley Interscience.

On the inference of large-scale magnetic fields on slowly rotating chemically peculiar stars, see

Deutsch, A.J. 1970, *Astrophys. J.*, **159**, 985,
Borra, E.F., Lanstreet, J.D., & Mestel, J. 1982, ARA&A, 20, 191,
Lanstreet, J.D. 2001, in *Magnetic field across the Hertzsprung-Russell diagram*, ASP Conf. Ser., vol. **248**, eds. G. Mathys, S.K. Solanki, and D.T. Wickramasinghe, 277,

and references therein. The flux rope dynamo of §7.2.2 is discussed and analyzed in

Vainshtein, S.I., & Zeldovich, Ya. B. 1972, *Soviet Physics Uspekhi*, **15**(2), 159.
Moffatt, H.K., & Proctor, M.R.E. 1985, *J. Fluid Mech.*, **154**, 493.

In addition, the mathematically-inclined will not want to miss the in-depth discussion of Stretch-Twist-Fold to be found in

Gilbert, A.D., 2003, "Dynamo theory", in *Handbook of Mathematical Fluid Dynamics*, vol. 2, eds. S. Frielander and D. Serre, Elsevier, 355-441,

from which Figure 7.4 was directly lifted. Magnetic flux expulsion from regions of closed streamlines is discussed in many textbooks dealing with magnetohydrodynamics. Analytical solutions for some specific cellular flows can be found for example in

Moffatt, H.K. 1978, *Magnetic field generation in electrically conducting fluids* (Cambridge: Cambridge University Press),
Parker, E.N. 1979, *Cosmical Magnetic Fields*, Oxford: Clarendon Press, chap. 16.

but for the first and last word on this topic, you should consult

Weiss, N.O. 1966, Proc. Roy. Soc. London A, 293, 310,
Rhines, P.B., & Young, W.R. 1983, J. Fluid Mech., 133, 133.

The Rhines & Young paper contains clean analytical examples of the two successive dissipative phases with characteristic timescales proportional to $\mathrm{R}_m^{1/3}$ and R_m, as discussed in §7.3.4. Flux expulsion is of course not restricted to 2-D flow; for a nice example in 3-D see

Galloway, D.J., & Proctor, M.R.E. 1983, *Geophys. Astrophys. Fluid Dyn.*, **24**, 109.

On the possible symmetrization of the Saturnian magnetic field by deep-seated differential rotation, see

Stevenson, D.J. 1982, *Geophys. Astrophys. Fluid Dyn.*, **21**, 113-127,
Kirk, R.L., & Stevenson, D.J. 1987, *Astrophys. J.*, **316**, 836-846.

An insightful discussion of the symmetrization process in more general terms is that of

Rädler, K.-H. 1986, On the effect of differential rotation on axisymmetric and non-axisymmetric magnetic fields in cosmic bodies, in *Proceedings of the Joint Varenna-Abastumani International School and Workshop*, ESA Spec. Pub. SP-251, 569-574.

As for planetary magnetic field observations, a good recent overview is

Connerney, J.E.P. 1993, *J. Geophys. Res.*, **98**, 18659-18679.

On anti-dynamo theorems, see

Cowling, T.G. 1933, *Mon. Not. Roy. Astron. Soc.*, **94**, 39,
Bullard, E.C., & Gellman, H., *Phil. Trans. R. Soc. London A*, **247**, 213,
Zeldovich, Ya. B. 1956, J. Exp. and Theoretical Physics, 31, 154 [Russian];
Zeldovich, Ya. B., & Ruzmaikin, A.A. 1980, J. Exp. and Theoretical Physics, 78, 980 [Russian];

as well as pages 113-ff and 538–ff, respectively, of the books by Moffatt and Parker listed above. English translations of the last two papers are also reprinted in *Selected Works of Yakov Borisovich Zeldovich*, vol. 1 (ed. J.P. Ostriker, Princeton, 1992).

Chapter 8

Fast and slow dynamos

It is nice to know that the computer understands the problem,
but I would like to understand it too.

Attributed to E.P. Wigner

In light of the anti-dynamo theorems considered in §7.4, our next move should be obvious: we need to consider three-dimensional flows and magnetic fields. In addition, another relevant class of flow not excluded by the theorems is that of time-dependent flows. In this chapter we focus on one example of each of these two potentially promising flow classes. These will in fact provide us with our first working dynamos.

The cell flow solution of the preceding chapter also illustrated the potentially dangerous role of boundary conditions in mimicking dynamo action. To bypass this difficulty, the flows (and magnetic fields) we consider in this chapter are chosen to be **spatially periodic**. Dynamo action, if and when it occurs, is then evidently a property of the flows themselves, rather than a boundary effect. Although this takes us somewhat farther away from the astrophysical context, much is to be learned about magnetic field amplification in electrically conducting fluids using such simplified models.

8.1 The Roberts cell dynamo

8.1.1 The Roberts cell

The Roberts cell is a spatially periodic, incompressible flow defined over a 2D domain $(x, y) \in [0, 2\pi]$ in terms of a stream function

$$\Psi(x, y) = \cos x + \sin y. \tag{8.1}$$

so that

$$\mathbf{u}(x, y) = \frac{\partial \Psi(x, y)}{\partial y}\hat{\mathbf{e}}_x - \frac{\partial \Psi(x, y)}{\partial x}\hat{\mathbf{e}}_y + \Psi(x, y)\hat{\mathbf{e}}_z \tag{8.2}$$

Note that the flow velocity is independent of the z-coordinate, even though the flow has a non-zero z-component. Equations (8.2)–(8.1) describes a periodic array of counterrotating flow cells in the $[x, y]$ plane, with a z-component that changes sign from one cell to the next; the total flow is then a series of helices, which have the same kinetic helicity $h = \mathbf{u} \cdot \nabla \times \mathbf{u}$ in each cell. The Roberts cell flow represents one example of a **Beltrami flows**, i.e., it satisfies the relation $\nabla \times \mathbf{u} = \alpha \mathbf{u}$, where α is a numerical constant. Such flows are **maximally helical**, in the sense that their vorticity ($\boldsymbol{\omega} \equiv \nabla \times \mathbf{u}$) is everywhere parallel to the flow, which maximizes helicity for a given flow speed.

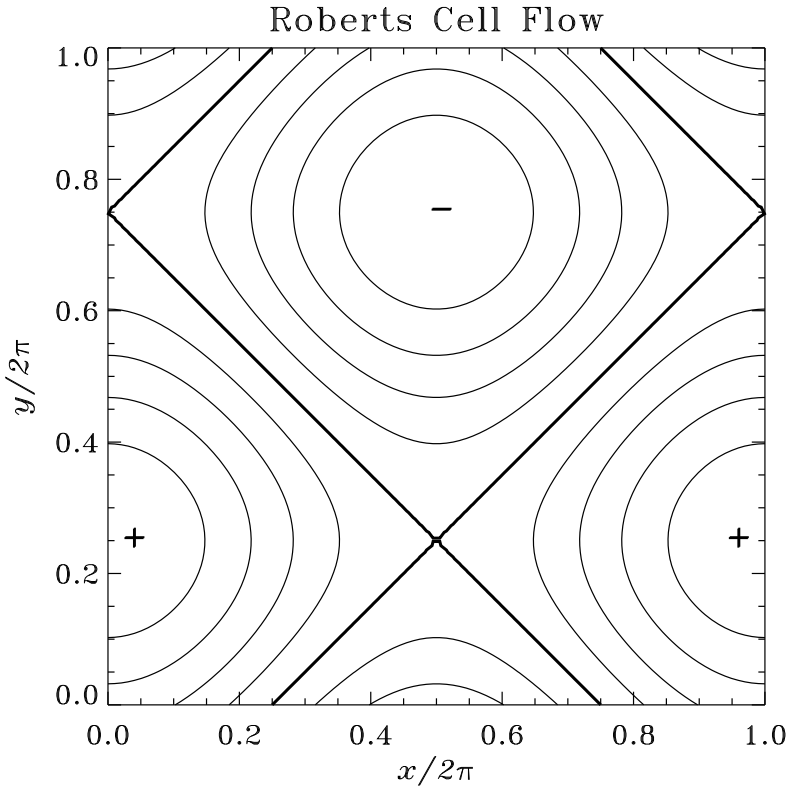

Figure 8.1: The Roberts cell flow. The flow is periodic in the $[x, y]$ plane, and independent of the z-coordinate (but $u_z \neq 0$!). Flow streamlines are shown projected in the $[x, y]$ plane, and the $+/-$ signs indicate the direction of the z-component of the flow. The thicker contour defines the network of **separatrix surfaces** in the flow, corresponding to cell boundaries. The u_z isocontours coincide with the projected streamlines.

Figure 8.1 shows one periodic "unit" of the the Roberts cell flow pattern. Note the presence of two **stagnation points** in the periodic cell, where four flow cells meet at $(x, y) = (0, 3\pi/2)$ and $(\pi, \pi/2)$. Let's first pause and consider why one should expect the Roberts cell to evade Cowling's and Zeldovich's theorems. First, note that this is not a planar flow in the sense demanded by Zeldovich's theorem, since we do have three non-vanishing flow components. However, the z-coordinate is ignorable in the sense of Cowling's theorem, since all flow components are independent of z. *If this flow is to evade Cowling's theorem and act as a dynamo, it must act on a magnetic field that is dependent on all three spatial coordinates.*

Consequently, we consider the inductive effects of this flow acting on a fully three dimensional magnetic field $\mathbf{B}(x, y, z, t)$. Since the flow speed is independent of z, we can expect solutions of the linear induction equation to be separable in z, i.e.:

$$\mathbf{B}(x, y, z, t) = \mathbf{b}(x, y, t)e^{ikz} \tag{8.3}$$

where k is a (specified) wavevector in the z-direction, and the 2D magnetic amplitude $\mathbf{b}$ is now a complex quantity. We are still dealing with a fully 3D magnetic field, but the problem has been effectively reduced to two spatial dimensions (x, y), which represents a great computational advantage.

8.1.2 Dynamo action at last

From the dynamo point of view, the idea is again to look for solutions of the induction equations where the magnetic energy does not fall to zero as $t \to \infty$. In practice this means specifying k, as well as some weak field as an initial condition, and solve the 2D linear initial value problem

for $\mathbf{b}(x,y,t)$ resulting from the substitution of eq. (8.3) into the induction equation:

$$\frac{\partial \mathbf{b}}{\partial t} = (\mathbf{b}\cdot\nabla_{xy})\mathbf{u} - (\mathbf{u}\cdot\nabla_{xy})\mathbf{b} - iku_z\mathbf{b} + \mathrm{R}_m^{-1}(\nabla_{xy}^2\mathbf{b} - k^2\mathbf{b}) \tag{8.4}$$

subjected to periodic boundary conditions on $\mathbf{b}$. Here ∇_{xy} and ∇_{xy}^2 are the 2D gradient and Laplacian operators in the $[x,y]$ plane. As before we use as a time unit the turnover time τ_c, which is of order 2π here. All solutions described below were obtained numerically using second order finite difference in both space and time.

The time evolution of the can be divided into three more or less distinct phases, the first two being similar to the case of the 2D cellular flow considered in the preceding chapter: (1) quadratic growth of the magnetic energy for $t \lesssim \tau_c$; (2) flux expulsion for the subsequent few τ_c. However, and unlike the case considered in §7.3, for some values of k the third phase is one of *exponential growth* in the magnetic field (and energy).

Figure 8.2 shows a typical Roberts cell dynamo solution, here for $\mathrm{R}_m = 10^2$ and $k = 2$. What is plotted is the real part of the z-component of $\mathbf{b}(x,y,t)$, at time $t \gg \tau_c$. The thick dashed lines are again the separatrices of the flow. One immediately recognizes the workings of flux expulsion, in that very little magnetic flux is present near the center of the flow cells. Instead the field is concentrated in thin sheets parallel to the separatrix surfaces. Given our extensive discussion of flux expulsion in the preceding chapter, it should come as no surprise that the thickness of those sheets scales as $\mathrm{R}_m^{-1/2}$. For $t \gg \tau_c$, the field grows exponentially, but the shape of the "planform" remains fixed. In other words, even though we solved the induction equation as an initial value problem, the solution can be thought of as an eigensolution of the form $\mathbf{B}(x,y,z,t) = \mathbf{b}(x,y)e^{ikz+st}$, with $\mathrm{Re}(s) > 0$ and $\mathrm{Im}(s) = 0$.

In terms of the magnetic energy evolution, the growth rate s of $\mathbf{b}(x,y,t)$ is readily obtained by a linear least-squares fit to the $\log \mathcal{E}_\mathrm{B}$ vs t curves in the $t \gg \tau_c$ regime, or more formally defined as

$$s = \lim_{t\to\infty}\left[\frac{1}{2t}\log(\mathcal{E}_\mathrm{B})\right]. \tag{8.5}$$

It turns out that the Roberts cell flows yields dynamo action (i.e., $s > 0$) over wide ranges of wavenumbers k and magnetic Reynolds number R_m. Figure 8.3 shows the variations in growth rates with k, for various values of R_m. The curves peak at a growth rate value k_max that gradually shifts to higher k as R_m increases. The largest growth rate is $k_\mathrm{max} \simeq 0.17$, and occurs at $\mathrm{R}_m \simeq 10$. It can be shown (see bibliography) that in the high R_m regimes the following scalings hold:

$$k_\mathrm{max} \propto \mathrm{R}_m^{1/2}, \qquad \mathrm{R}_m \gg 1\ , \tag{8.6}$$

$$s(k_\mathrm{max}) \propto \frac{\log(\log \mathrm{R}_m)}{\log \mathrm{R}_m}, \qquad \mathrm{R}_m \gg 1\ . \tag{8.7}$$

To understand the origin of these peculiar scaling relations, we need to take a closer look at the mechanism through which the magnetic field is amplified by the Roberts cell.

8.1.3 Exponential stretching and stagnation points

Even cursory examination of Figure 8.2 suggests that magnetic field amplification in the Roberts cell is somehow associated with the network of separatrices and stagnation points. It will prove convenient in the foregoing analysis and discussion to first introduce new coordinates

$$x' = x - y\ , \qquad y' = x + y + \frac{3\pi}{2}\ , \tag{8.8}$$

corresponding to a $3\pi/2$ translation in the y-direction, followed by 45° rotation about the origin in the $[x,y]$ plane. The separatrices are now parallel to the coordinate lines $x' = n\pi$, $y' = n\pi$

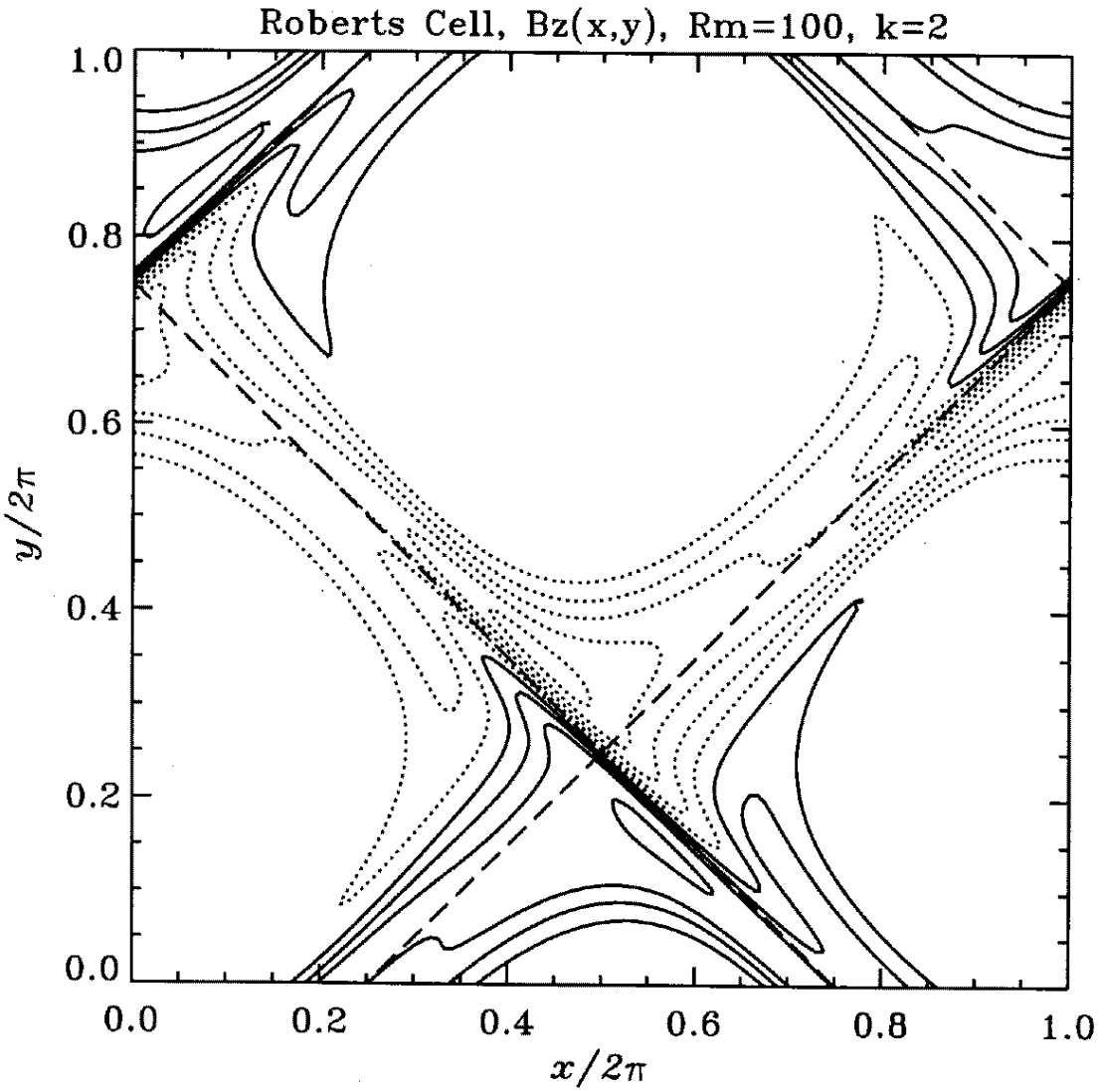

Figure 8.2: Isocontours for the z-component of the magnetic field in the $[x, y]$ plane, for a solutions with $R_m = 100$ and $k = 2$, in the asymptotic regime $t \gg \tau_c$. The dashed straight lines indicate the separatrix surfaces of the underlying Roberts cell flow (see Fig. 8.1). Note the flux expulsion from the cell centers, and the concentration of the magnetic flux in thin sheets pressed against the separatrices. In the $t \gg \tau_c$ regime, the field grows exponentially but the shape of the planform is otherwise steady.

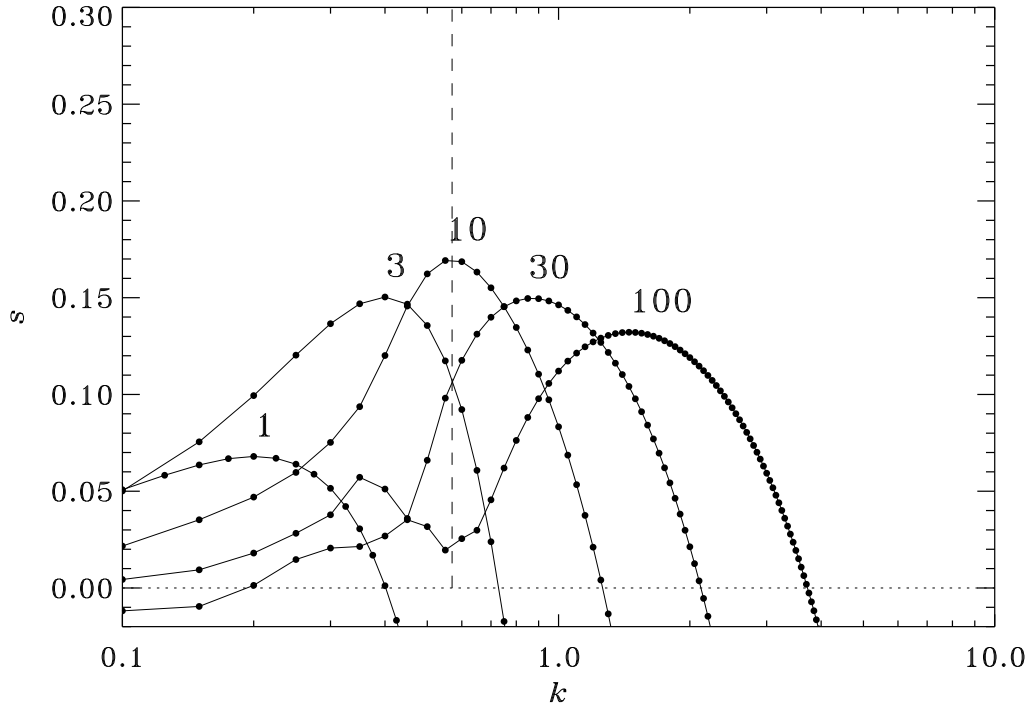

Figure 8.3: Growth rates of the magnetic energy in the Roberts cell, for sequences of solutions with increasing k and various values of R_m, as labeled near the maxima of the various curves. Growth typically occurs for a restricted range in k, and peaks at a value $k_{\max}$ that increases slowly with increasing R_m. Note however how the corresponding maximum growth rate decreases with increasing R_m. The small "dip" left of the main peaks for the high-R_m solutions is a real feature, although here it is not very well resolved in k.

$(n = 0, 1, ...)$, and the stream function has become

$$\Psi(x', y') = 2\sin(x')\sin(y') \ . \tag{8.9}$$

Close to the stagnation points, a good approximation to eq. (8.9) is

$$\Psi(x', y') \simeq 2x'y' \ , \qquad x', y' \ll 1 \tag{8.10}$$

which, if anything else, should now clarify why this is called a hyperbolic stagnation point... Consider now a fluid element flowing in the vicinity of this stagnation point. From a Lagrangian point of view its equations of motion are:

$$\frac{\partial x'}{\partial t} = u_{x'} = 2x' \ , \tag{8.11}$$

$$\frac{\partial y'}{\partial t} = u_{y'} = -2y' \ , \tag{8.12}$$

which immediately integrates to

$$x'(t) = x'_0 e^{2t}, \qquad y'(t) = y'_0 e^{-2t} \ , \tag{8.13}$$

where (x'_0, y'_0) is the location of the fluid element at $t = 0$. Evidently, the fluid element experiences **exponential stretching** in the x'-direction, and corresponding contraction in

the y'-direction (since $\nabla \cdot \mathbf{u} = 0$!). Now, recall that in ideal MHD ($\mathrm{R}_m = \infty$) a magnetic fieldline obeys an equation identical to that of a line element, and that stretching leads to field amplification as per the mass conservation constraint (§7.2.1). Evidently stagnation point have quite a bit of potential, when it comes to amplifying exponentially a pre-existing magnetic field... providing that diffusion and destructive folding can be held at bay.

8.1.4 Mechanism of field amplification in the Roberts cell

We have shown that the Roberts cell can act as a dynamo, and that the field amplification mechanism is intimately tied to the presence of hyperbolic stagnation points at the cell corners. What we still need to do is figure out how the magnetic field generated by the Roberts cell manages to evade destructive folding.

We stick to the rotated Roberts cell used above, restrict ourselves to the $\mathrm{R}_m \gg 1$ regime, and pick up the field evolution after flux expulsion is completed and the magnetic field is concentrated in thin boundary layers (thickness $\propto \mathrm{R}_m^{-1/2}$) pressed against the separatrices (as on Fig. 8.2).

Consider a x'-directed magnetic fieldline crossing a vertical separatrix, as shown on Figure 8.4A (gray line labeled "a"). the y' component of the flow is positive on either side of the separatrix, and peaks on the separatrix. Consequently, the fieldline experiences stretching in the y'-direction ($a \to b \to c \to d$ on Fig. 8.4A). However, the induced y' component of the magnetic field changes sign across the separatrix, so that we seem to be heading towards our dreaded destructive folding. This is where the crucial role of the vertical (z) dimension becomes apparent. Figure 8.4B is a view of the same configuration in the $[x', z]$ plane, looking down onto the y' axis on part A. At $t = 0$ the fieldlines have no component in the z-direction, but in view of the assumed e^{ikz} spatial dependency the x' component changes sign every half-wavelength k/π. Consider now the inductive action of the z-component of the velocity, which changes sign across the separatrix. After some time interval of order $k/(\pi u_z)$ the configuration of Fig. 8.4B will have evolved to that shown on part C. Observe what has happened: the fieldlines have been sheared in such a way that y'-components of the magnetic field of like signs have been brought in close proximity. Contrast this to the situation on part B, where magnetic footpoints in closest proximity have oppositely directed y'-components.

The end result of this process is that a y'-directed magnetic field is produced by shearing of the initial x'-directed field, with a phase shift in the z-direction such that destructive folding is avoided. Clearly, this requires *both* a z-component of velocity, *and* a z-dependency in the magnetic field. Either alone won't do the trick.

Now, the same reasoning evidently applies to a y'-directed magnetic fieldline crossing a horizontal separatrix: a x'-directed magnetic field will be induced. That magnetic field will be swept along the horizontal separatrix, get further amplified by exponential stretching as it zooms by the stagnation point, and continue along the vertical separatrix, where it can now serve as a seed field for the production of a y'-directed field. The dynamo "loop" is closed, at any time the rate of field production is proportional to the local field strength, and exponential growth of the field follows. The process works best if the half wavelength k/π is of order of the boundary layer thickness, which in fact is what leads to the scaling law given by eq. (8.6). The scaling for the growth rate (eq. (8.7)), in turn, is related to the time spent by a fluid element in the vicinity of the stagnation point.

8.2 Fast versus slow dynamos

One noteworthy aspect of the Roberts cell dynamo is the general decrease of the growth rates with increasing R_m (see Fig. 8.3). This is worrisome, because the $\mathrm{R}_m \to \infty$ limit is the one relevant to most astrophysically interesting circumstances. A dynamo exhibiting this property is called a **slow dynamo**, in contrast to a **fast dynamo**, which (by definition) retains a finite growth rate as $\mathrm{R}_m \to \infty$. In view of eq. (8.7), the Roberts cell is thus formally a slow dynamo.

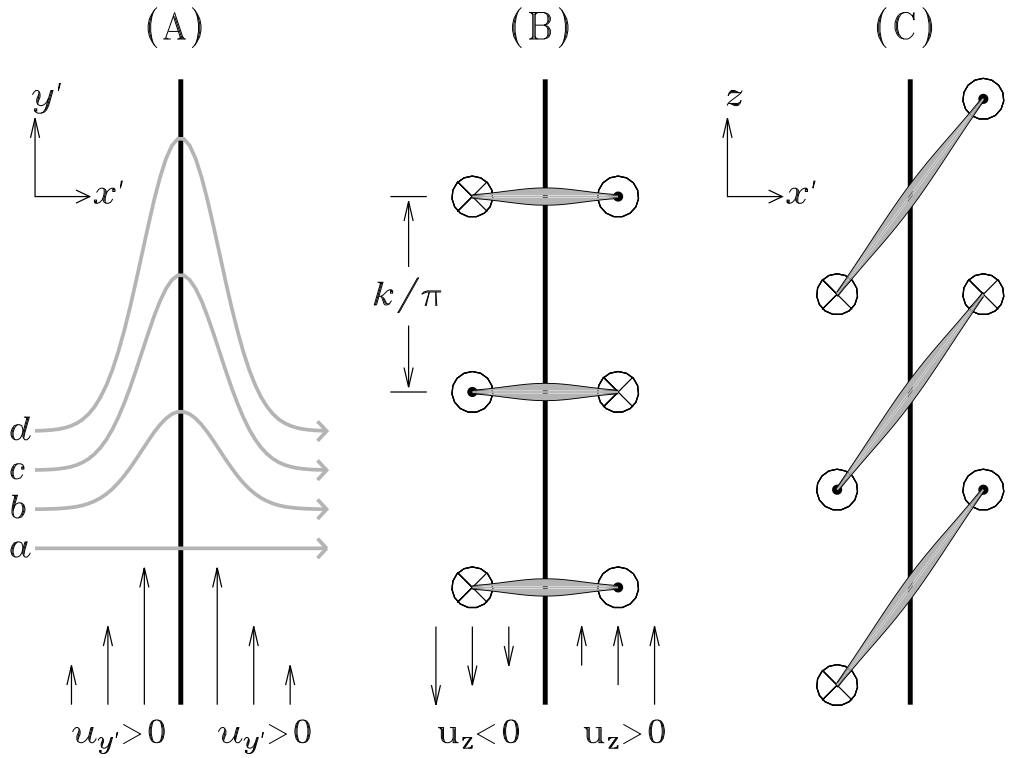

Figure 8.4: Mechanism of magnetic field amplification in the Roberts cell flow. The diagram is plotted in terms of the rotated $[x', y']$ Roberts cell. The thick vertical line is a separatrix surface, and the gray lines are magnetic fieldlines. Part (A) is a view in the horizontal plane $[x', y']$, and shows the production of a y'-directed magnetic component from an initially x'-directed magnetic field (line labeled "a"). Parts (B) and (C) are views in the $[x', z]$ plane looking down along the y' axis, and illustrate the phase shift in the z-direction of the y' magnetic component caused by the z-component of the velocity. The symbol $\odot$ ($\otimes$) indicates a magnetic field coming out (into) the plane of the page. Note on part (C) how footpoints of identical polarity are brought in close proximity, thus avoiding the destructive folding that would have otherwise characterized the situation depicted on part B in the $u_z = 0$ 2D case.

However the RHS of eq. (8.7) is such a slowly decreasing function of R_m that the Roberts cell is arguably the closest thing it could be to a fast dynamo... without formally being one. The distinction hinges on the profound differences between the strict mathematical case of $\mathrm{R}_m = \infty$ (ideal MHD), and the more physically relevant limit $\mathrm{R}_m \to \infty$.

8.2.1 The singular limit $\mathrm{R}_m \to \infty$

From the physical point of view, the distinction between strict ideal MHD ($\eta = 0$) and the $\eta \to 0$ limit (or, equivalently, $\mathrm{R}_m \to \infty$) is a crucial one. One example will suffice. Recall that in the absence of dissipation **magnetic helicity** is a conserved quantity in any evolving magnetized fluid:

$$\frac{\mathrm{d}\mathcal{H}_\mathrm{B}}{\mathrm{d}t} = \frac{\mathrm{d}}{\mathrm{d}t}\int_V \mathbf{A}\cdot\mathbf{B}\,\mathrm{d}V = 0, \tag{8.14}$$

where $\mathbf{B} = \nabla \times \mathbf{A}$. Dynamo action, (in the sense of amplifying a weak initial field) is then clearly impossible except for the subset of initial fields having $\mathcal{H}_\mathrm{B} = 0$. This is a very stringent constraint on dynamo action! Go back now to the Roberts cell dynamo in the high-R_m regime. We saw that magnetic structures builp up on a horizontal length scale $\propto \mathrm{R}_m^{-1/2}$, and that the vertical wavelength of the fastest growing mode also decreases as $\mathrm{R}_m^{-1/2}$. *The inexorable shrinking of the length scales ensures that dissipation always continue to operate in the* $\mathrm{R}_m \to \infty$ *limit.*. This is why the Roberts cell dynamo can evade the constraint of helicity conservation. This is also why it is a slow dynamo. On the other hand, the Vainshtein & Zeldovich Stretch-Twist-Fold dynamo of §7.2, with its growth rate $\sigma = \ln 2$, is a fast dynamo since nothing prevents it from operating in the $\mathrm{R}_m \to \infty$ limit.

But is this really the case? In the flows we have considered up to now, the existence of dynamo action hinges on stretching winning over destructive folding; in the 2D cellular flow of §7.3, destructive folding won over stretching everywhere away from boundaries. In the Roberts cell, destructive folding is avoided only for vertical wavenumbers such that magnetic fields of like signs are brought together, minimizing dissipation. The STF dynamo actually combines stretching and constructive folding, such that folding *reinforces* stretching. The fact that destructive folding is avoided entirely is why the growth rate does not depend on R_m.

Well, upon further consideration it turns out that magnetic diffusivity must play a role in the STF rope dynamo after all. Diffusion comes in at two levels; the first and most obvious one is at the "knot" formed by the STF sequence. The second and less obvious arises from the fact that as one applies the STF operation n times, the resulting "flux rope" is in fact made up of n closely packed flux ropes, each of cross-section $\propto 2^{-n}$ times smaller than the original circular flux rope, so that the total cross-section looks more like a handful of spaghettis that it does a single monolithic flux rope of strength $\propto 2^n$. If one waits long enough, the magnetic length scale perpendicular to the loop axis shrinks to zero, so that even in the $\mathrm{R}_m \to \infty$ limit dissipation is bound to come into to play.

8.3 Fast dynamo action: the CP flow

Knotty pasta notwithstanding, and despites its cartoon nature, the STF dynamo exemplifies the importance of constructive folding for fast dynamo action. However, it turns out to be exceedingly difficult (though possible, see bibliography) to find a smooth, continuous flow than achieves the requires stretch-twist-fold action. Fortunately, there exists wide classes of relatively simple (and analytically expressible) flows that, at least in the kinematic regime, achieves something essentially similar. In this section, we concentrate on one such flow, the so-called CP flow (for "Circularly Polarized"), as a prototypical flow yielding fast dynamo action.

8.3.1 The CP flow

The CP flow is nothing more than our familiar Roberts cell flow, with one important twist: an explicit time dependency is introduced in the flow:

$$u_x(x,y,t) = A\cos(y + \epsilon\sin\omega t) \ , \tag{8.15}$$

$$u_y(x,y,t) = C\sin(x + \epsilon\cos\omega t) \ , \tag{8.16}$$

$$u_z(x,y,t) = A\sin(y + \epsilon\sin\omega t) + C\cos(x + \epsilon\cos\omega t) \ . \tag{8.17}$$

What we have now is a periodic array of maximally helical counterotating flow cells, as on Fig. 8.1, with all cells "precessing" in unison in the $[x,y]$ plane along circular paths of radius ϵ, undergoing a full revolution in a time interval $2\pi/\omega$ [1]. In what follows we set $\omega = 1$, $\epsilon = 1$, $A = C = \sqrt{3/2}$, without any loss of generality.

The time-dependence of the flow turns out to have profound consequences for particle trajectories. Figure 8.5 shows the distances between two particles whose trajectories are being followed in the CP flow and in the the Roberts cell flow of §8.1, for the same starting positions and over the same time interval. The differences are striking. The short line element initially joining the two particles is stretched exponentially in the CP flow, but lengthens more or less linearly with time in the Roberts cell, as shown by the two fits on Figure 8.5.

Now, exponential streching, or, equivalently, exponential divergence of initially neighbouring trajectories, is the hallmark of **chaos**. Chaos has generated much hype (and occasional nonsense) in the literature, but the mathematical concept of chaos turns out to be extremely useful in analyzing flows for (potential) fast dynamo action.

8.3.2 Measures of chaos

The usefulness of chaos lies here with the fact that it can offer "measures" of fast dynamo action, without actually having to solve the induction equation! We now briefly consider two graphical measures of chaos: **Poincaré sections** and **Lyapunov exponents**.

A Poincaré section of the CP flow is shown on Figure 8.6. It is constructed by launching tracer particles at $z = 0$ (and $t = 0$), and following their trajectories as they are carried by the flow. At every 2π time interval, the position of the particle is plotted in the $[x,y]$ plane (modulo 2π in x and y, since most particles leave the original 2π-domain within which they were released). Some particles never venture too far away from their starting position in the $[x,y]$ plane. They end up tracing close curves (the so-called **KAM tori**, after Kolmogorov, Arnold, and Moser). Those curves, however distorted they may end up looking, identify regions of space where trajectories are integrable. Other particles, on the other hand, never return to their starting position. If one waited long enough, one such particle would eventually come arbitrarily close to all points in the $[x,y]$ plane outside of the integrable regions. The corresponding particle trajectory is said to be **space filling**, and the associated particle motion *chaotic*. The region of the $[x,y]$ plane defined by the starting positions of all particles with space filling trajectories is called the *chaotic region* of the flow. [2].

Poincaré sections are useful to quickly eyeball the size of chaotic regions for a given set of flow parameters, but have little quantitative predictive values as to the potential efficiency of the flow as a dynamo. For this the **Lyapunov exponent** turns out to be a more useful quantity. The Lyapunov exponent is another fancy name for a rather simple concept; one, moreover that we encountered already on Fig. 8.5: the rate of exponential divergence of two

[1] It is left as an (easy) exercise to verify that this is yet another Beltrami flow, and to figure out the form of the time-dependent stream function that describes it.

[2] Try sketching (or computing) a Poincaré section for the time-independent Roberts cell flow of §8.1. Does it differ much from Fig. 8.6?

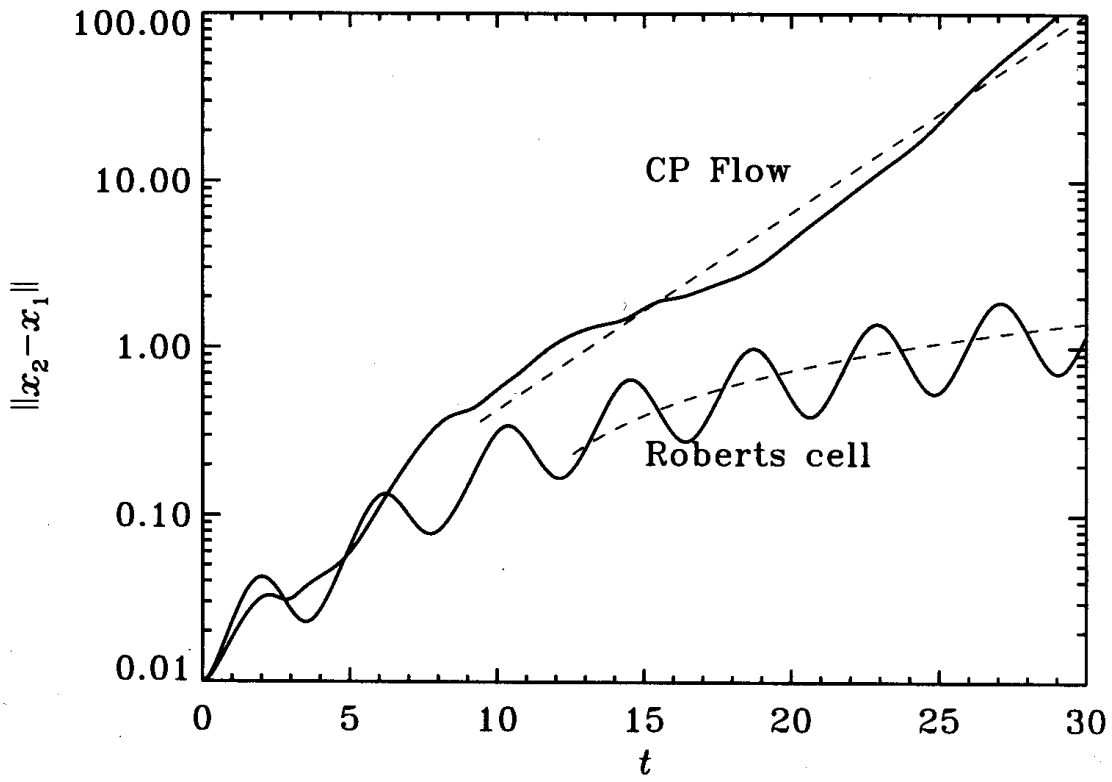

Figure 8.5: Stretching of a short line element initially located in the $z = 0$ plane, and "released" at $t = 0$ in the CP flow or Roberts cell. The two dashed lines are: (1) a linear least-squares fit of $\log ||x_2 - x_1||$ vs t to the CP flow curve, indicating *exponential* stretching; a linear least-squares of $||x_2 - x_1||$ vs t for the Roberts cell trajectory, indicating *linear* stretching.

neighbouring fluid element located at $\mathbf{x}_1$, $\mathbf{x}_2$ at $t = 0$ somewhere in the flow. The Lyapunov exponent λ_L can be (somewhat loosely) defined via

$$\ell(t) = \ell(0) \exp(\lambda_L t) \ , \tag{8.18}$$

where $\ell \equiv \|\mathbf{x}_2 - \mathbf{x}_1\|$ is the length of the *tangent vector* between the two fluid elements. Conceptually, Λ_L is nothing more than the slope of the dotted line on Fig. 8.5! Note however that, in general, Λ_L is likely to be a function of the position and relative orientations of $\mathbf{x}_1$ and $\mathbf{x}_2$. Strictly speaking Λ_L is mathematically defined in terms of stretching of an *infinitesimal* line element, located at a and oriented in direction e:

$$\lambda_L = \lim_{t\to\infty} \left(\frac{1}{2t} \log(\Lambda_{ij} e_i e_j) \right) \tag{8.19}$$

where

$$\Lambda_{ij} = \frac{\partial x_k}{\partial a_i} \frac{\partial x_k}{\partial a_j} \tag{8.20}$$

is the rate of strain tensor, so that $\Lambda_{ij} e_i e_j$ is the square of the stretching factor at time t. Because there are three independent possible directions in 3D space, one can compute *three* distinct Lyapunov exponents at any given point in the flow, and it can be shown that for an incompressible flow their sum is zero[3]. Now, the important thing about Lyapunov exponents is that $\lambda_L > 0$ somewhere in the flow indicates that this flow has chaotic regions.

[3]Demonstrate this result. Hint: start by thinking about what happens in the vicinity of a simple stagnation point, such as in §8.1.3

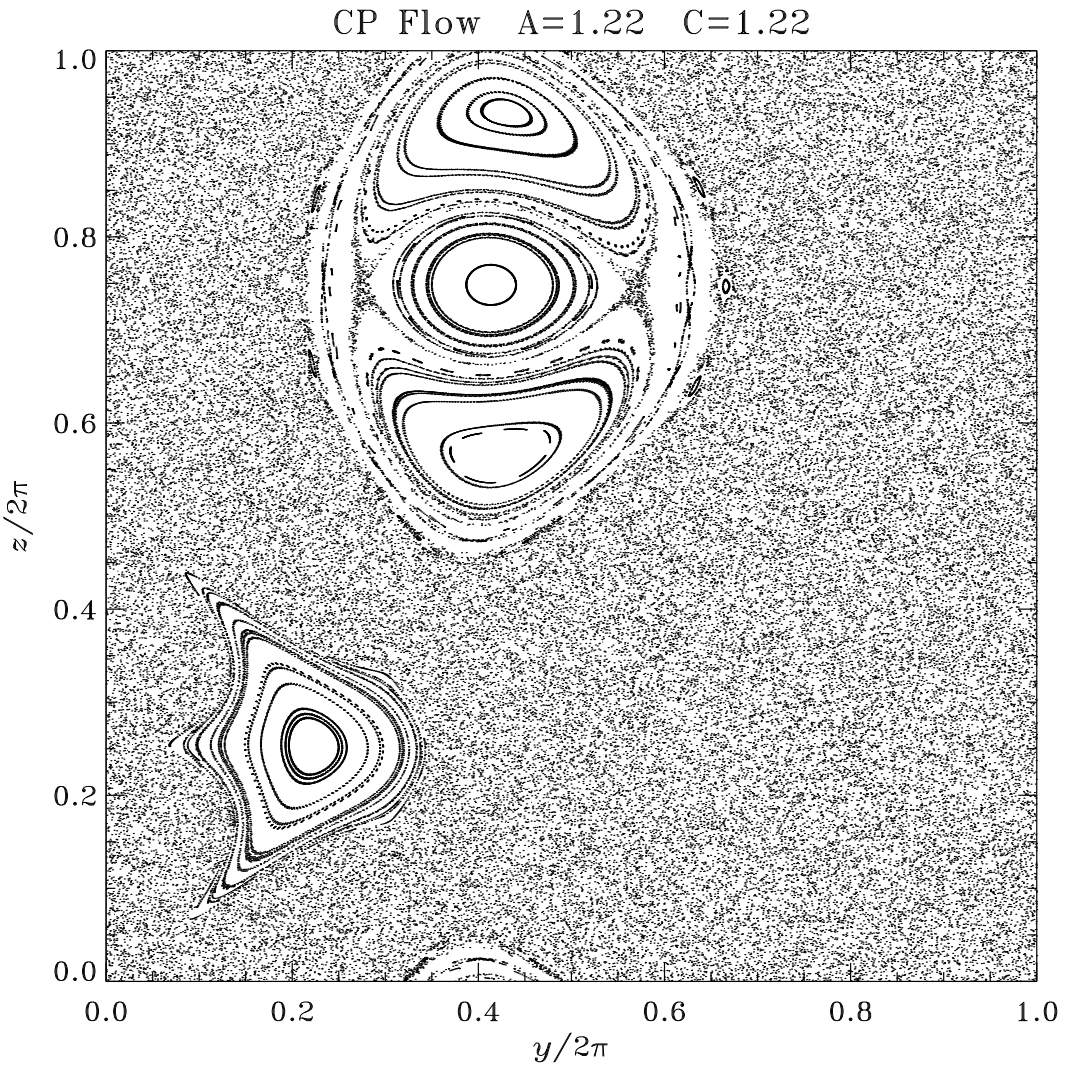

Figure 8.6: Poincaré section for the CP flow, for $\epsilon = 1$, $\omega = 1$, and $A = C = \sqrt{3/2}$. The plot is constructed by repeatedly "launching" particles at $z = 0$, $t = 0$, following their trajectories in time, and plotting their (projected) position (modulo 2π) in the $[x, y]$ plane at interval $\Delta t = 2\pi$. The flow is chaotic within the featureless "salt-and-pepper" regions, and integrable in regions threaded by close curves.

Numerically, Lyapunov exponents are most often computed by repeatedly launching a set of particles defining a short line segment, advecting them over a finite time t, and measuring the rate of exponential stretching of that line segment by summing the (exponentially increasing) distances between successive particles. The procedure is repeated for particle pairs with varying starting positions and relative orientations. Figure 8.7 shows a map $\Lambda_L(x,y)$ of the *largest* Lyapunov exponent for the CP flow as a function of position in the $[x,y]$ plane. The dark regions correspong to $\Lambda_L(x,y) \leq 0$, and the bright salt-and-pepper regions to $\Lambda_L(x,y) > 0$. The absolute largest Lyapunox exponent is $\Lambda_L^{\max} = 1.45$ here. Comparing Figure 8.7 to the Poincaré section on Fig. 8.6, one observes some definite similarities. For example, the integrable KAM regions on the Poincaré section correspond roughly to dark regions on the Lyapunov map. Yet the correspondence is far from perfect, illustrating the fact that trajectories and stretching of line elements are two related, but nonetheless distinct beasts.

8.3.3 Necessary conditions for fast dynamo action

Figures 8.6 and 8.7 might be aesthetically pleasing, but do they teach us anything *quantitative* about fast dynamo action? The Lyapunov exponent certainly does. There exists two important theorems stating that

1. A smooth flow cannot be a fast dynamo if $\lambda_L = 0$, so that $\lambda_L > 0$, or, equivalently, the existence of chaotic regions in the flow, is a necessary (although not sufficient) condition for fast dynamo action;

2. In the limit $\mathrm{R}_m \to \infty$, the largest Lyaponuv exponent of the flow is an upper bound on the dynamo growth rate.

Proofs of these theorems need not concern us here (but see bibliography). The theorems are indeed very useful information, in that they allows us to *rule out* fast dynamo action in many classes of flows. However, if one wants to *prove* fast dynamo action in a flow, at this writing there is no option but to integrate the induction equation. Time to return to the CP flow and do just that.

8.3.4 Fast dynamo action

Our search for dynamo action in the CP flow closely parallels what we did in the context of the Roberts cell. The time-dependency of the CP flow does not preclude the existence of solutions separable in z, so we again express the magnetic field via eq. (8.3), and solve the 2D induction equation (8.4) as an initial-boundary value problem, for specified vertical wavenumbers k. Periodic boundary conditions are again imposed on $\mathbf{b}(x,y,t)$. The time variation of the magnetic energy is again used as a test of dynamo action, and a growth rate is computed using eq. (8.5) for solutions exhibiting exponential growth in the $t \gg \tau_{\mathrm{c}}$ regime.

As with the Roberts cell, dynamo action (i.e., positive growth rates $s(k,\mathrm{R}_m)$) occur in a finite range of vertical wavenumber k. Once again the phase of exponential growth sets in after a time of order of the turnover time. Figure 8.8 is similar in format to Fig. 8.2, and shows isocontours of the vertical magnetic field $b_z(x,y,t)$ in the phase of exponential growth, for a $\mathrm{R}_m = 2000$ solutions with $k = 0.57$. The solution is fully time-dependent, and its behavior is best appreciated by viewing it as an animation[4]. The solution is characterized by multiple sheets on intense magnetic field, of thickness once again $\propto \mathrm{R}_m^{-1/2}$.

The CP flow solution of Fig. 8.8 exhibits **spatial intermittency**. If one were to randomly choose a location somewhere in the $[x,y]$ plane, chances are good that only a weakish magnetic field would be found. In high-R_m solutions, strong fields are concentrated in small regions of the domain; in other words, their **filling factor** is small. This can be quantified by computing the **probability density function** (hereafter PDF) of the magnetic field strength, $f(|B_z|)$.

[4] which you can do, of course, on the course's Web Page, and for a few R_m values, moreover...

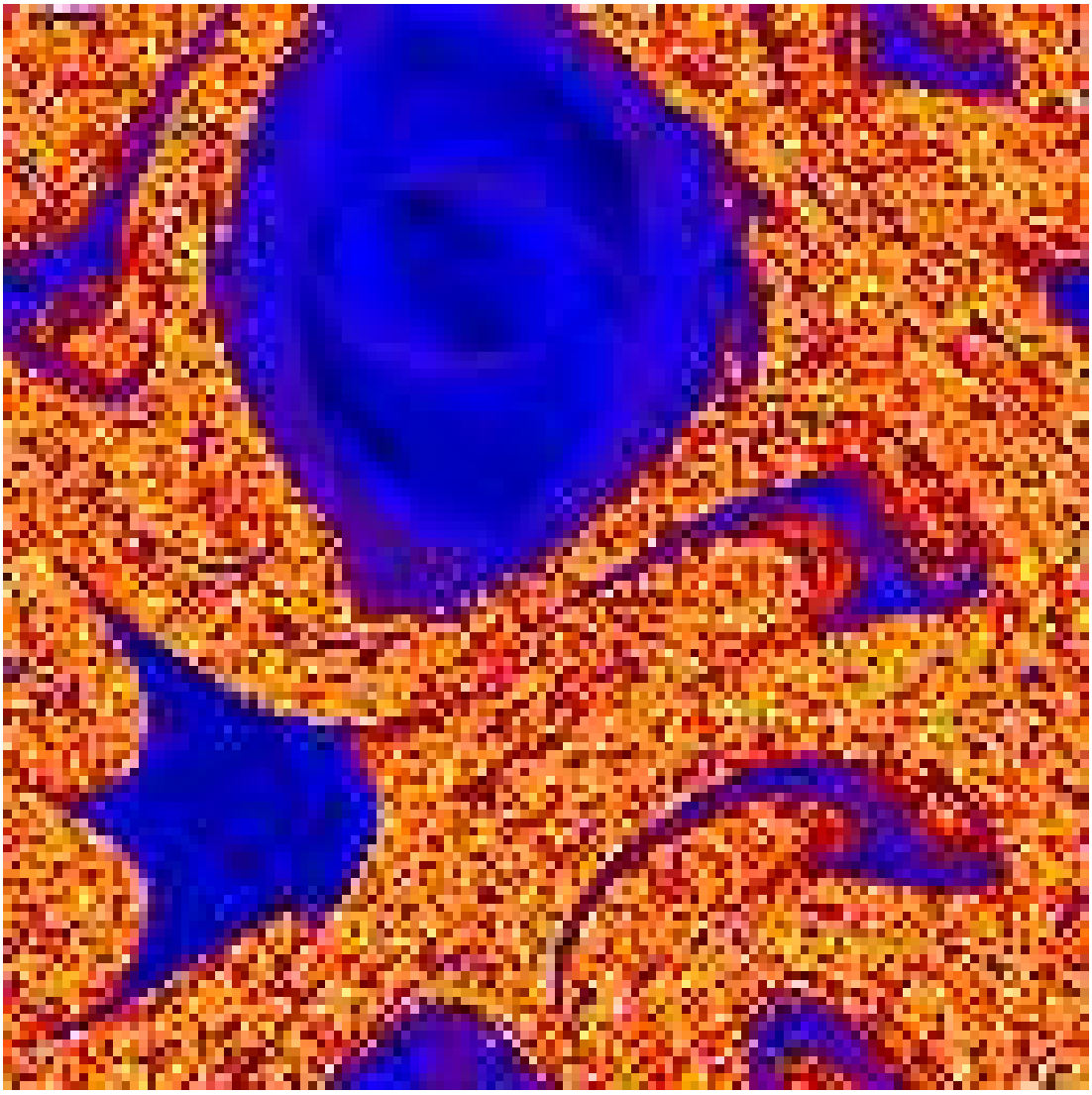

Figure 8.7: Finite time Lyaponuv exponent map for the CP flow with $\epsilon = 1$, $\omega = 1$, and $A = C = \sqrt{3/2}$. The dark part of the color scale correspond to negative Λ_L, and the brighter regions to $\Lambda_L > 0$. Compare this map to the Poincaré section of Figure 8.6.

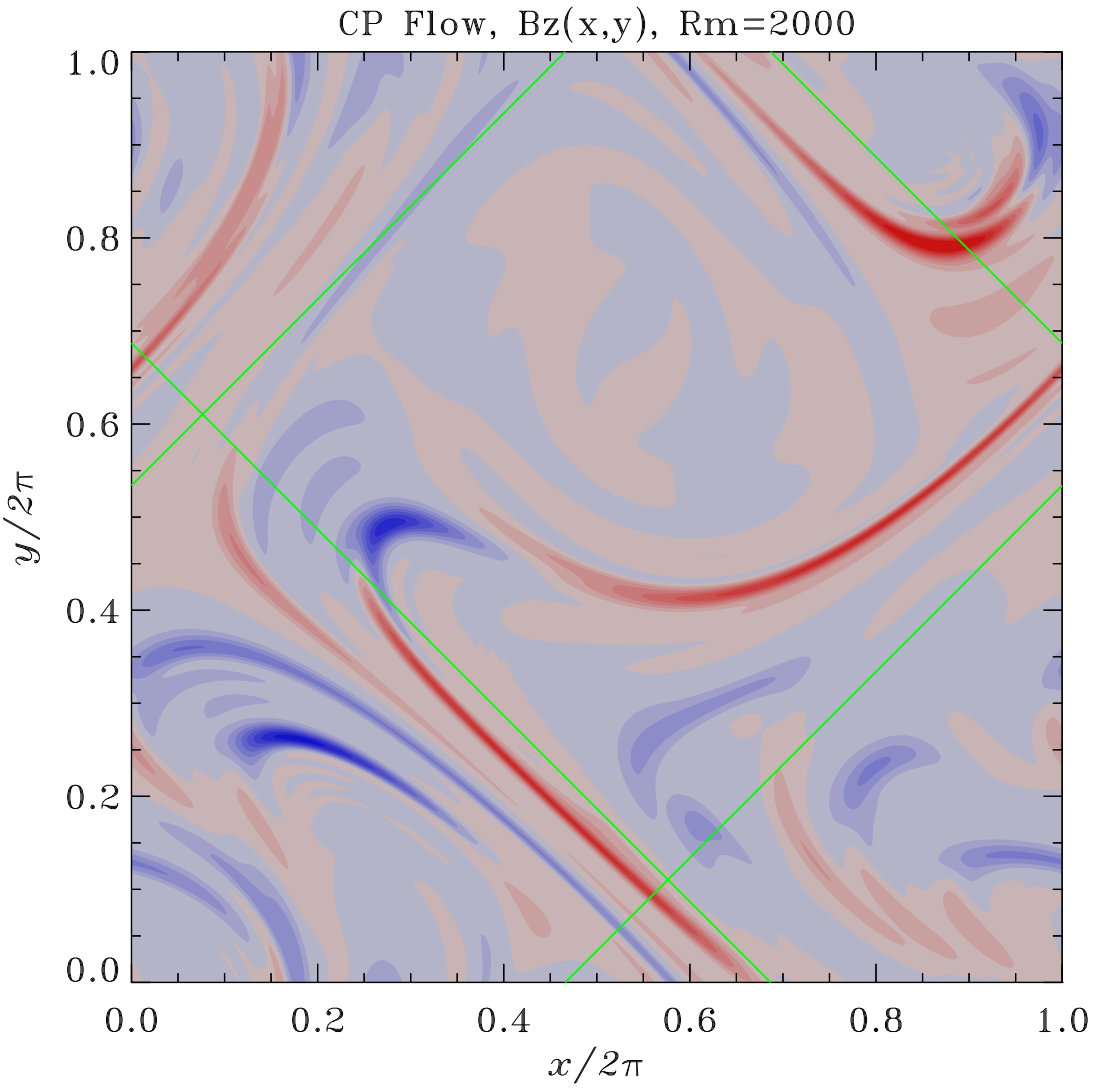

Figure 8.8: Snapshot of the z-component of the magnetic field in the $[x, y]$ plane, for a CP Flow solution with $R_m = 2000$ and $k = 0.57$, in the asymptotic regime $t \gg \tau_c$. The color scale codes the field strength (gray-to-blue is negative, gray-to-red positive). The green straight lines indicate the separatrix surfaces of the underlying Roberts cell flow (see Fig. 8.1). Unlike the Roberts cell solution of Fig. 8.2, this is a strongly time-dependent solution, although still exhibiting overall exponential growth of the magnetic field.

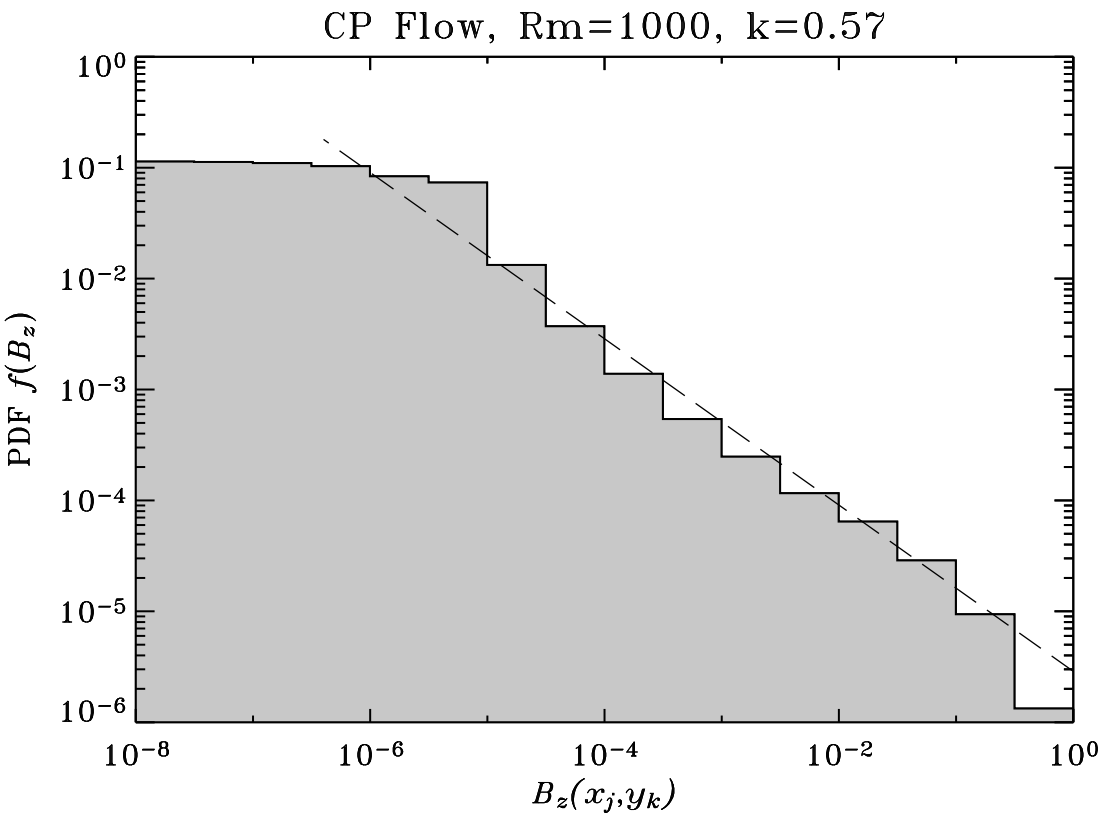

Figure 8.9: Probability density function for the (unsigned) strength of the z-component of the magnetic field, for a $\mathrm{R}_m = 10^3$, $k = 0.57$ CP flow dynamo. The peak field strength has been normalized to a value of unity. Note the power-law tail at large field strength (straight line in this log-log plot, with slope ~ -0.75).

This involves measuring B_z at every (x, y) mesh point in the solution domain, and simply counting how many mesh points have $|B_z|$ between values B and $B + \mathrm{d}B$. The result of such a procedure is shown in histogram form on Figure 8.9. The PDF shows a power-law tail at high field strengths,

$$f(|B_z|) \propto |B_z|^{-\gamma} , \qquad |B_z| \gtrsim 10^{-5} , \tag{8.21}$$

spanning over four orders of magnitude in field strength, and with $\gamma \sim 1$ here. This indicates that strong field are still far more likely to be detected than if the magnetic field was simply a normally-distributed random variable (for example)[5]. The fact that the PDF's logarithmic slope is flatter than -2 indicates that the *largest* local field strength found in the domain will always dominate the computation of the spatially-averaged field strength[6].

The CP flow dynamo solutions also exhibit **temporal intermittency**; if one sits at one specific point (x, y) point in the domain and measures B_z at subsequent time steps, a weak B_z is measured most of the time, and only occasionally are large values detected. Once again the PDF shows a power-law tail with slope flatter than -2 indicating that a temporal average of B_z at one location will always be dominated by the largest B_z measured to date[7].

Unlike in the Roberts cell, the range of k yielding dynamo action does *not* shift significantly to higher k as R_m is increased, and in the high R_m regime the corresponding maximum growth

[5]What would be the shape of a Gaussian PDF on a log-log plot such as Fig. 8.9?

[6]Prove this; it begins with writing down an certain integral involving the PDF that yields the average value the variable of interest.

[7]Could you make an educated guess at the value of the logarithmic slope of this temporal PDF?

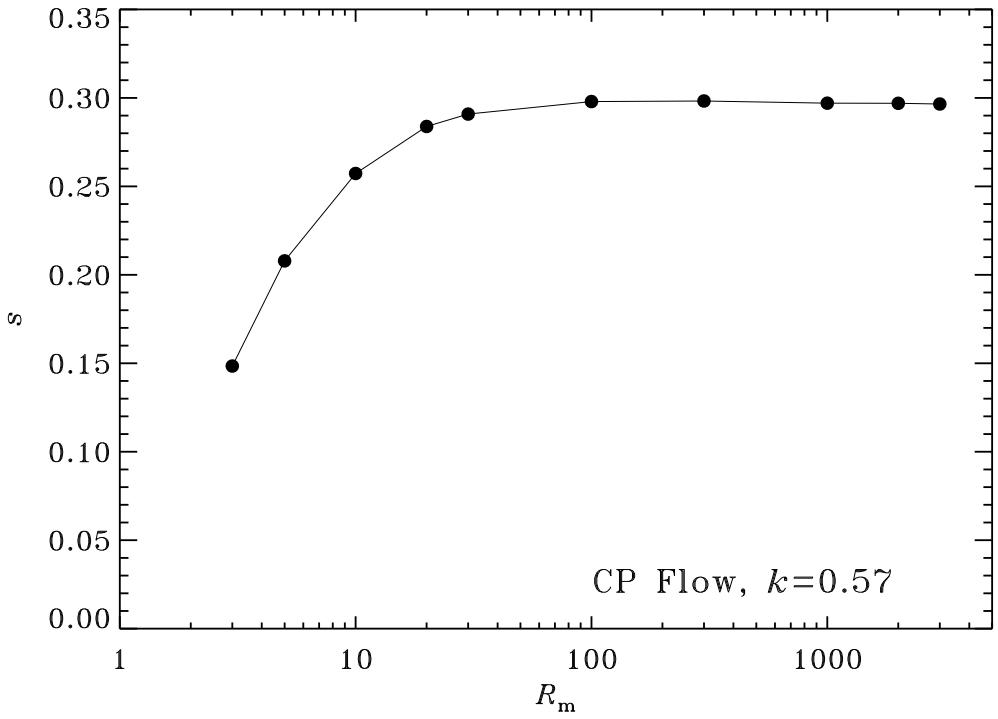

Figure 8.10: Growth rate of $k = 0.57$ CP flow dynamo solutions, plotted as a function of the magnetic Reynolds number (solid line). The constancy of the growth rate in the high-R_m regime suggests (but does not strictly prove) that this dynamo is fast.

rate $k_{\max}$ does *not* decrease with increasing R_m (see Fig. 8.3). In the CP flow considered here ($A = C = \sqrt{3/2}$, $\omega = 1$, $\epsilon = 1$), $k_{\max} \simeq 0.57$, with $s(k_{\max}) \simeq 0.3$ for $\mathrm{R}_m \gtrsim 10^2$, as shown on Figure 8.10 (solid line). Figure 8.10 suggests (but does not rigorously prove!) that the CP flow acts as a fast dynamo, since by all appearances

$$\lim_{\mathrm{R}_m \to \infty} s(k_{\max}) > 0 \ . \tag{8.22}$$

8.3.5 Magnetic flux versus magnetic energy

With the CP flow, we definitely have a pretty good dynamo on our hands. But how are those dynamo solutions to be related to the Sun (or other astrophysical bodies)? So far we have concentrated on the magnetic energy as a measure of dynamo action, but in the astrophysical context **magnetic flux** is also important. Consider the following two (related) measures of magnetic flux:

$$\Phi = \mid \langle \mathbf{B} \rangle \mid \ , \qquad F = \langle \mid \mathbf{B} \mid \rangle \ , \tag{8.23}$$

where the angular brackets indicate some sort of suitable spatial average over the whole computational domain. The quantity Φ is nothing but the average magnetic flux, while F is the average **unsigned flux**. Under this notation the magnetic energy can evidently be written as $\mathcal{E}_{\mathrm{B}} = \left\langle \mid \mathbf{B} \mid^2 \right\rangle$. Consider now the scaling of the two following ratios as a function of the magnetic Reynolds number:

$$\mathcal{R}_1 = \frac{\mathcal{E}_{\mathrm{B}}}{\Phi^2} \propto \mathrm{R}_m^n \ , \tag{8.24}$$

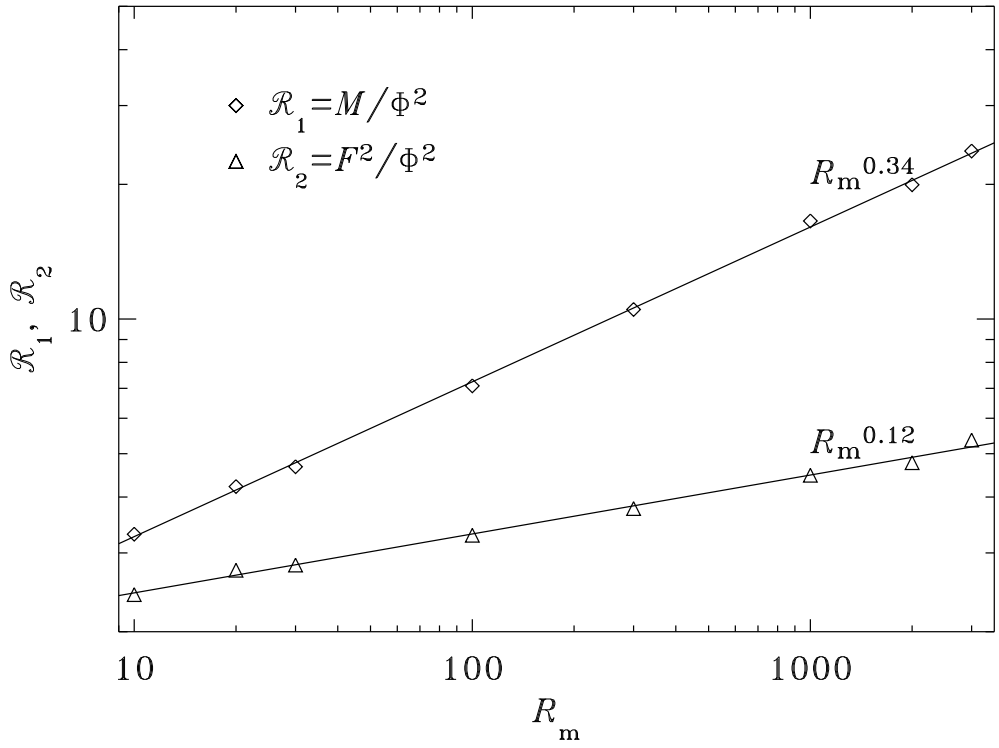

Figure 8.11: Variations with R_m of the two ratios defined in eqs. (8.24)–(8.25). Least squares fits (solid lines) yield power law exponents $n = 0.35$ and $\kappa = 0.13$.

$$\mathcal{R}_2 = \frac{F^2}{\Phi^2} \propto \mathrm{R}_m^{\kappa} \ . \tag{8.25}$$

A little reflection will reveal that a large value of $\mathcal{R}_1$ indicates that the magnetic field is concentrated in a small total fractional area of the domain, i.e., the **filling factor** is much smaller than unity[8]. The ratio $\mathcal{R}_2$, on the other hand, is indicative of the dynamo's ability to generate a net signed flux. The exponent κ measures the level of **folding** in the solution; large values of κ indicate that while the dynamo may be vigorously producing magnetic flux on small spatial scales, it does so in a manner such that very little *net* flux is being generated on the spatial scale of the computational domain. Figure 8.11 shows the variations with R_m of the two ratios defined above. Least squares fits to the curves yields $n = 0.35$ and $\kappa = 0.13$. Positive values for the exponents κ and n indicate that the CP flow dynamo is relatively inefficient at producing magnetic flux in the high R_m regime, and even less efficient at producing net signed flux. While other flows yielding fast dynamo actions lead to different values for these exponents, in general they seem to always turn out positive, with $\kappa < n$, so that the (relative) inability to produce net signed flux seems to be a generic property of fast dynamos in the high-R_m regime.

8.3.6 Fast dynamo action in the nonlinear regime

We conclude this section by a brief discussion of fast dynamo action in the nonlinear regime. Evidently the exponential growth of the magnetic field will be arrested once the Lorentz force becomes large enough to alter the original CP flow. What might the nature of the backreaction on **u** look like?

[8]If you can't figure it out try this: take a magnetic field of strength B_1 crossing a surface area A_1; now consider a more intense magnetic field, of strength $B_2 = 4B_1$, concentrated in one quarter of the area A_1; calculate $\mathcal{E}_\mathrm{B}$, Φ, and $\mathcal{R}_1$... get it?

Naively, one might think that the Lorentz force will simply reduce the amplitude of the flow components, leaving the overall geometry of the flow more or less unaffected, i.e., $\mathbf{u}_1 \simeq \mathbf{u}_0$. That this cannot be the case becomes obvious upon recalling that in the high R_m regimes the eigenfunction is characterized by magnetic structures of typical thickness $\propto \mathrm{R}_m^{-1/2}$, while the flow has a typical length scale $\sim 2\pi$ in our dimensionless units. The extreme disparity between these two length scales in the high-R_m regime suggests that the saturation of the dynamo-generated magnetic field will involve alterations of the flow field on small spatial scales, so that a flow very much different from the original CP flow is likely to develop in the nonlinear regime.

That this is indeed what happens was was nicely demonstrated some years ago by F. Cattaneo and collaborators (see references in bibliography), who computed simplified nonlinear solutions of dynamo action in a suitably forced CP flow. They could show that

1. the r.m.s. flow velocity in nonlinear regime is comparable to that in the original CP flow;
2. magnetic dissipation actually *decreases* in the nonlinear regime;
3. dynamo action is suppressed by the disappearance of chaotic trajectories in the nonlinear flow.

8.4 The solar small-scale magnetic field

Of course, the problem with small-scale solar magnetic fields is precisely that—they *are* small-scale. And being small-scale makes them very difficult to resolve. Being unresolved, in truth there is not a lot one can discover about them, even with current state-of-the-art high precision spectropolarimetry.

All flows yielding dynamo actions that have been considered up to now are very artificial, and are arguably more akin to malfunctioning washing machines than any sensible astrophysical object. Nonetheless some of the things we have learned do carry over to more realistic circumstances. Most importantly, fast dynamos

1. produce flux concentrations on scales $\propto \mathrm{R}_m^{-1/2}$;
2. produce little or no mean-field, i.e., signed magnetic flux on a spatial scale comparable to the size of the system;
3. require chaotic flow trajectories to operate.

As a kind of proof of these sweeping statements, consider Figure 8.12 herein. It is a snapshot of a numerical simulation of dynamo action in a stratified, thermally-driven turbulent fluid being heated from below, and spatially periodic in the horizontal directions. This flow acts as a vigorous nonlinear fast dynamo, with a ratio of magnetic to kinetic energy of about 20%. The Figure shows a snapshot of the vertical magnetic field component $B_z(x, y)$ essentially at the top of the simulation box[9].

Thermally convecting flows in a stratified background have long been known to be characterized by cells of broad upwellings of warm fluid. These cells have a horizontal size set by, among other things, the density scale height within the box; On the other hand, the downwelling of cold fluid needed to satisfy mass conservation end up being concentrated in a network of narrow lanes at the boundaries between adjacent upwelling cells. This asymmetry is due to the vertical pressure and density gradient in the box: rising fluid expands laterally into the lower density layers above, and descending fluid is compressed laterally in the higher density layers below. Near the top of the simulation box, this leads to the concentration of magnetic structures in the downwelling lanes, as they are continuously being swept horizontally away from the centers of upwelling cells. This is the origin of the cellular pattern so striking on Fig. 8.12.

[9] ...and, as usual, you can view an animation of this simulation on the course Web Page.

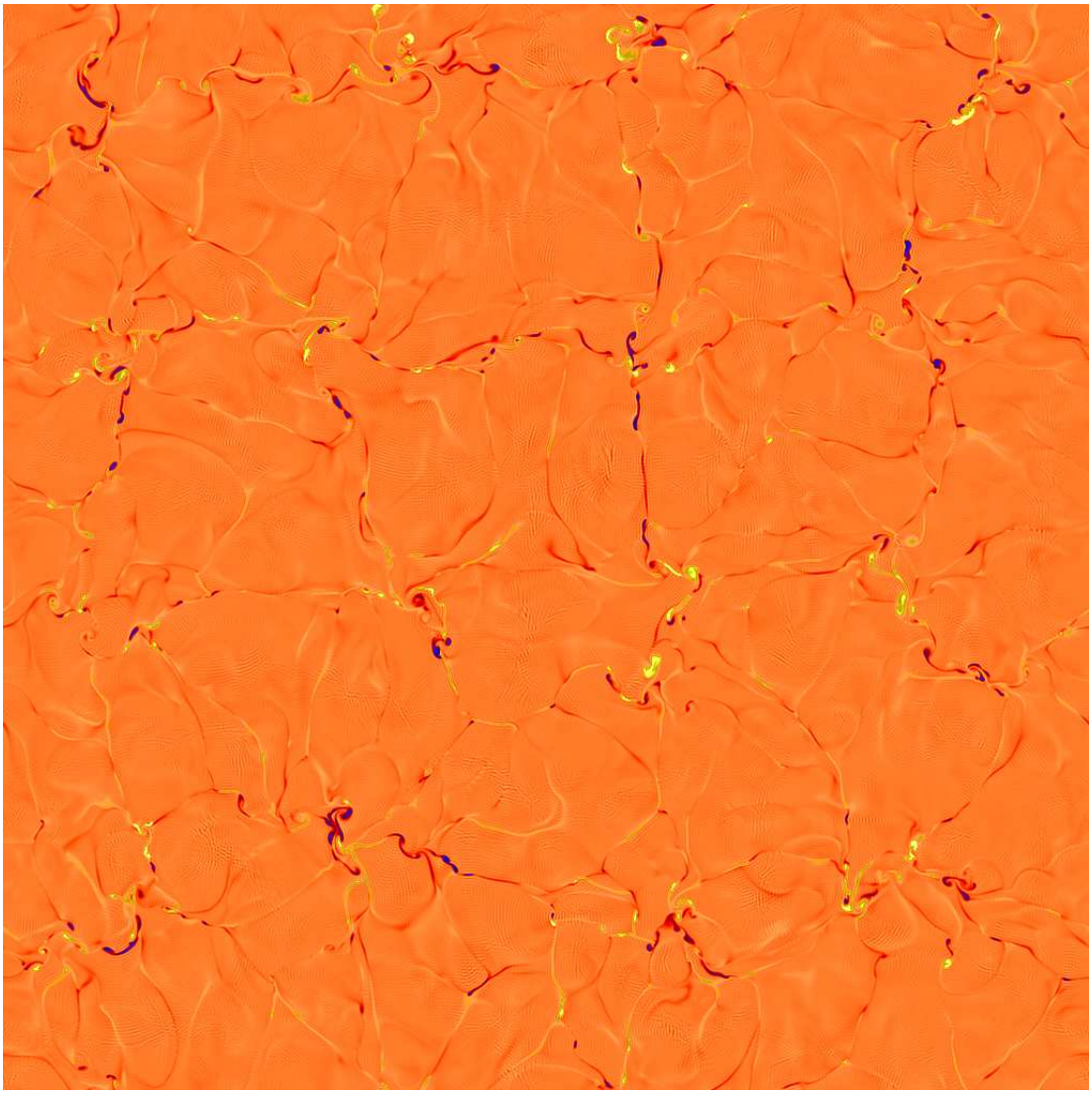

Figure 8.12: Snapshot of the top "horizontal" $[x, y]$ plane of a MHD numerical simulation of thermally-driven stratified turbulent convection in a box of aspect ratio $x : y : z = 10 : 10 : 1$, at a Viscous Reynolds number of 245 and $\mathrm{R}_m = 1225$. The simulation uses a pseudo-spectral spatial discretrization scheme, with 1024 collocation points in the x and y directions, and 97 in z. The color scale encodes the vertical (z) component of the magnetic field (orange-to-yellow is positive B_z, orange-to-blue negative). Numerical simulation results kindly provided by F. Cattaneo, University of Chicago.

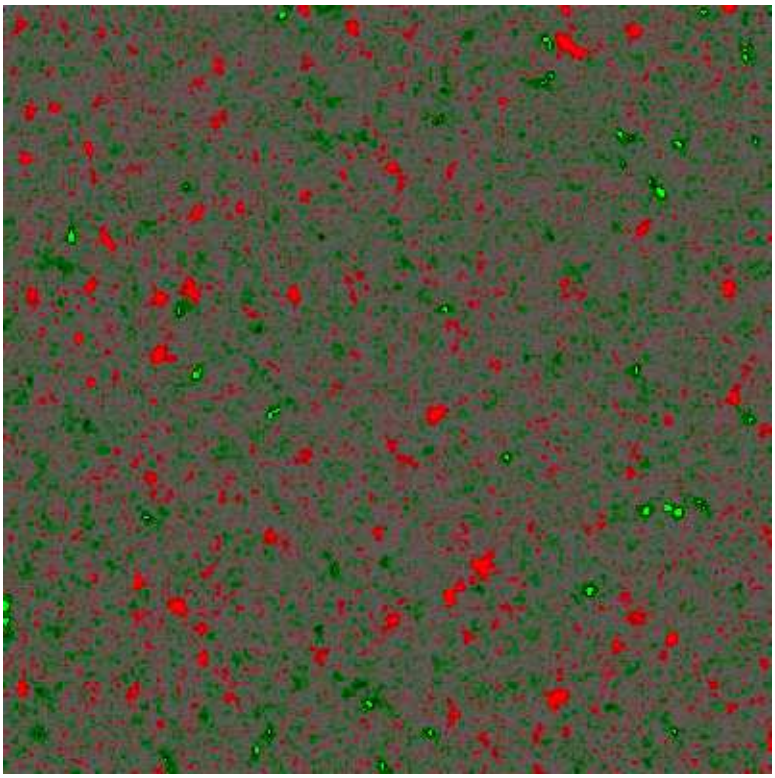

Figure 8.13: High resolution magnetogram (0.6 arcsec/pixel) of a small piece of "quiet sun", obtained my the MDI instrument onboard SOHO. The color scale encodes the line-of-sight component of the magnetic field, with red/green corresponding to positive/negative magnetic polarities

While this flow is far more complex (spatially and temporally) than the Roberts cell or CP flow, is exhibits some of the characteristics we have already encountered in the context of these simpler flows:

1. The magnetic field is highly intermittent, both spatially and temporally.
2. Magnetic flux concentrations are found on scales $\propto \mathrm{R}_m^{-1/2}$;
3. little or no **mean** magnetic field is produced on the scale of the computational box.

The fundamental physical link between this MHD simulation and the CP flow is the presence of chaotic trajectories in the flow, which in both cases is the culprit behind fast dynamo action.

Now consider figure 8.13 which shows a high-resolution magnetogram of a small piece of the solar photosphere, far away from sunspots or active regions. Note how the magnetic field is spatially very intermittent, and seems to have no marked preference for negative (black) or positive (white), except perhaps for the plage-like structure in the upper left corner. Here also the magnetic field is very intermittent, both spatially and temporally[10]. This is all *qualitatively* similar to the field distribution characterizing Fig. 8.12.

Fast dynamo action therefore offers an attractive explanation for the *small-scale* solar magnetic fields. Nice and fine, but the Sun also has a fairly well-defined large-scale component, for which something else than fast dynamo action must then be invoked. It turns out that

[10] A magnetogram animation can be viewed on the course web page, and illustrates quite well the temporally intermittent nature of the solar small-scale magnetic field.

the turbulent nature of the flow in the solar convective envelope can still do the trick, but to examine this we will need to adopt as statistical approach to turbulence and to the associated flow-field interactions. This is the focus of the following chapter.

Problems:

1. Calculate $\nabla \cdot \mathbf{u}$ and $\nabla \times \mathbf{u}$ for the Roberts Cell flow. Confirm that it is a Beltrami flow, in the sense discussed in §8.1.

2. This problem aims at getting you to investigate in more detail what can happen to a magnetic field in the vicinity of a stagnation point. Consider the 2D cartesian incompressible flow defined by the stream function

$$\Psi(x, y) = u_0 xy \tag{8.26}$$

so that $u_x(x) = u_0 x$ and $u_y(y) = -u_0 y$ (note that the quantity u_0 has then units of s^{-1}!). We now want to consider the inductive action of this flow on a purely horizontal magnetic field, held fixed at values of $+B_0$ and $-B_0$, at $y = +L$ and $-L$ respectively. Evidently, this flow will tend to push the magnetic field towards the x-axis, where dissipation will occur since the field is oppositely directed on either side of the x-axis.

   (a) Show that the above flow has a stagnation point at the origin, and that its divergence is zero.

   (b) Show that in view of the imposed boundary condition, B_x can only be a function of the y coordinate everywhere in the domain $-L \leq y \leq +L$, $-\infty \leq x \leq \infty$.

   (c) Show that under these circumstances the x-component of the induction equation reduces to

$$\frac{1}{u_0}\frac{\partial B_x}{\partial t} = B_x + y\frac{\partial B_x}{\partial y} + \frac{\eta}{u_0 L}\frac{\partial^2 B_x}{\partial y^2},$$

   where lengths are expressed in units of L.

   (d) Show now that this equation accepts steady-state solutions of the form

$$B_x(y) = C\exp\left(-\alpha y^2\right) + D\exp\left(-\alpha y^2\right)\int_0^y \exp\left(\alpha(y')^2\right)\mathrm{d}y'$$

   where the parameter $\alpha = u_0 L^2/2\eta \equiv \mathrm{R}_m/2$ controls the relative importance of magnetic dissipation, as measured by the usual magnetic Reynolds number $\mathrm{R}_m = u_0 L/\eta$, and C and D are integration constants.

   (e) Show that the assumed boundary conditions imply that $C = 0$ here;

   (f) Now show that the thickness of the current sheet forming in the vicinity of $y = 0$ scales as $1/\sqrt{\alpha}$;

   (g) Evaluate numerically the integral on the above solution for $B_x(y)$ and plot the variation of B_x as a function of y, for values of $\alpha = 10, 100$ and 10^3.

   (h) Finally, compute the magnitude of the electric current in the z-direction, and show that the rate of energy dissipation is independent of the assumed value of η. Explain this physically.

3. The so-called ABC flow is another long-time candidate for fast dynamo action. It is a steady periodic flow in cartesian geometry, defined as

$$\mathbf{u}(x, y, z) = (A\sin z + C\cos y, B\sin x + A\cos z, C\sin y + B\cos x)$$

(a) Verify whether or not this is a Beltrami flow;

(b) Find the position(s) of the stagnation point(s) in the flow, for the specific case $A = B = C = 1$.

(c) Calculate a Poincaré section for this flow, using now parameter values $A = 1+$(your birth month/12), $B = 1+$(your birth day/30), $C = 1$. This involves repeatedly launching a particle somewhere on the $z = 0$ plane, and plotting its position at every crossing of $2\pi n$ planes in the z-direction ($n = 1, 2, ...$). Is this flow chaotic?

4. The flow near the 3D stagnation points in the ABC flow can be approximated in cylindrical polar coordinates (r, θ, z) by

$$\mathbf{u} = (\alpha r/2, 0, -\alpha z) \ ,$$

with $\alpha = \pm\sqrt{2}$.

(a) Calculate the the three Lyapunov exponents for $\alpha = +\sqrt{2}$ and $\alpha = -\sqrt{2}$, and show that in both cases their sum is zero.

(b) Obtain a solution to the steady ($\partial/\partial t = 0$) form of the induction equation, with $\mathbf{u}$ given by the above expression.

(c) On the basis of your solution, where would you expect to find magnetic fields in the flow?

(d) Again on the basis of your solution, estimate a length scale characterizing the thickness of the magnetic structures present in the solutions. How does this characteristic length scale with the magnetic Reynolds number?

5. This problem gets you to compute and compare the PDFs associated with the CP flow solution discussed in detail in this chapter, and the numerical simulation of Cattaneo *et al.* discussed in §8.4. First go to the Course Web Page, and grab the two data files containing snapshots of $B_z(x, y)$ for a CP flow solution, and for the turbulent dynamo solution plotted on Fig. 8.12.

(a) Compute the mean signed and unsigned fluxes for the two solutions; how do the corresponding ratii Φ/F compare?

(b) Compute the PDFs of $|B_z|$ in both cases, and compare/contrast their shape. How similar are they? Is this surprising? Why?

Bibliography:

The mathematical aspects of fast dynamo theory are discussed at length in the book

Childress, S., & Gilbert, A.D. 1995, *Stretch, Twist, Fold: The Fast Dynamo*, (Berlin: Springer),

although the reader prefering a shorter introduction might want to first work through the two following review articles:

Childress, S. 1992, in *Topological Aspects of the Dynamics of Fluids and Plasmas*, eds. H.K. Moffatt *et al.*, Kluwer, 111-147.

Soward, A.M. 1994, in *Lectures on Solar and Planetary Dynamos*, eds. M.R.E. Proctor & A.D. Gilbert, Cambridge University Press, 181.

as well as the recent review paper by A.D. Gilbert cited in the bibliography of the preceeding chapter. On the Roberts cell dynamo, see chapter 5 of the Childress & Gilbert book cited above, as well as

Roberts, G.O. 1972, *Phil. Trans. R. Soc. London*, A**271**, 411,
Soward, A.M. 1983, *J. Fluid Mech.*, **180**, 267.

The scaling relations given by eqs. (8.6)–(8.7) are derived in the Soward paper.

On dynamo action in the CP flow see

Galloway, D.J., & Proctor, M.R.E. 1992, *Nature*, **356**, 691,
Ponty, Y., Pouquet, A., & Sulem, P.L. 1995, *Geophys. Astrophys. Fluid Dyn.*, **79**, 239,
Cattaneo, F., Kim, E.-J., Proctor, M.R.E., & Tao, L. 1995, *Phys. Rev. Lett.*, **75**, 1522.

For all you would ever want to know about PDFs with power law tails, their statistical properties, and the mechanisms producing them, see the first few chapters in

Sornette, D. 2000, *Critical phenomena in natural sciences*, Springer.

The discussion in §8.3.5 follows closely that in the Cattaneo *et al.* (1995) paper cited above, with the results shown on Fig. 8.11 taken directly from that paper. On dynamo action in the ABC flow (problem 3.3), see

Galloway, D.J., & Frisch, U. 1984, *Geophys. Astrophys. Fluid Dyn.*, **29**, 13,
Galloway, D.J., & Frisch, U. 1986, *Geophys. Astrophys. Fluid Dyn.*, **36**, 53.

The mathematically inclined reader wishing to delve deeper into the theorems for fast dynamo action mentioned in §8.3 will get a solid and character building workout out of

Vishik, M.M. 1989, *Geophys. Astrophys. Fluid Dyn.*, **48**, 151,
Klapper, I., & Young, L.S. 1995, *Comm. Math. Phys.*, **173**, 623.

Our discussion of nonlinear effects in the CP flow is taken directly from

Cattaneo, F., Hughes, D.W., & Kim, E.-J. 1996, *Phys. Rev. Lett.*, **76**, 2057.

On dynamo action in three-dimensional thermally-driven convective turbulence, see

Cattaneo, F. 1999, *Astrophys. J.*, **515**, L39,
Cattaneo, F., Emonet, T., & Weiss, N.O. 2003, *Astrophys. J.*, **588**, 1183-1198.

The numerical simulation results shown on Fig. 8.12 are taken from the second of these papers.

The detection and statistics of small-scale magnetic flux concentrations has garnered much attention over the years. As the both resolution and sophistication of the detection methods improve, the picture continues to evolve and ideas must be discarded or recycled. The following chronological list of papers illustrates this process,

Spruit, H.C., & Zwaan, C. 1981, *Solar Phys.*, **70**, 207,
Zwaan, C. 1987, *Ann. Rev. Astron. Ap.*, **25**, 83,
Topka, K.P., et al. 1992, *Astrophys. J.*, **396**, 351,
Keller, C.U. 1992, Nature, **359**, 307,
Berger, T.E., et al. 1995, *Astrophys. J.*, **454**, 531,
Lin, H. 1995, *Astrophys. J.*, **446**, 421,
Berger, T.E., & Title, A.M. 1996, *Astrophys. J.*, **463**, 365,
Grossman-Doerth, U., et al. 1996, *Astron. Ap.*, **315**, 610,
Schrijver, C.J., et al. 1997, *Astrophys. J.*, **487**, 424.
Simon, G.W., Title, A.M., & Weiss, N.O. 2001, *Astrophys. J.*, **561**, 427.
Tsuneta, S., Ichimoto, K., Katsukawa, Y., and 11 co-authors 2008, *Astrophys. J.*, , in press.